Characterising the Behaviour of an Electromagnetic Levitation Cell using Numerical Modelling

by

Suzanne Roberts

Master's degree dissertation

Supervisor: Prof Schalk Kok
Co-supervisors: Dr Johan Zietsman & Dr Helen Inglis

Faculty of Engineering, Built Environment and Information Technology
Department of Mechanical and Aeronautical Engineering
University of Pretoria
South Africa

20 December 2016

Characterising the Behaviour of an Electromagnetic Levitation Cell using Numerical Modelling

Suzanne Roberts

Abstract

Experimental investigations of high temperature industrial processes, for example the melting and smelting processes taking place inside furnaces, are complicated by the high temperatures and the chemically reactive environment in which they take place. Fortunately, mathematical models can be used in conjunction with the limited experimental results that are available to gain insight into these high temperature processes. However, mathematical models of high temperature processes require high temperature material properties, which are difficult to measure experimentally since container materials are often unable to withstand high enough temperatures, and sample contamination often occurs. These difficulties can be overcome by employing containerless processing techniques such as electromagnetic levitation melting to allow for characterisation of high temperature material properties.

Efficient design of electromagnetic levitation cells is challenging since the effects of changes in coil design, sample size and sample material on levitation force and sample temperature are not yet well understood. In this work a numerical model of the electromagnetic levitation cell is implemented and used to investigate the sensitivity of levitation cell operation to variations in coil design, sample material and sample size.

Various levitation cell modelling methods in literature are reviewed and a suitable model is chosen, adapted for the current application, and implemented in Python. The finite volume electromagnetic component of the model is derived from Maxwell's equations, while heat transfer is modelled using a lumped parameter energy balance based on the first law of thermodynamics. The implemented model is verified for a simple case with a known analytical solution, and validated against published experimental results. It is found that a calibrated model can successfully predict the lifting force inside the levitation cell, as well as the sample temperature at low coil currents.

The validated model is used to characterise the operation of a levitation cell for a number of different sample materials and sample sizes, and for variations in coil geometry and coil current. The model can be used in this way to investigate a variety of cases and hence to support experimental levitation cell design. Based on model results, a number of operating procedure recommendations are also made.

Contents

List of Figures

List of Tables

List of Symbols

$'$	Source point
$\dot{Q}$	Heat transfer [W]
ϵ_0	Permittivity of free space $[C^2/Nm^2]$
η	Kinematic viscosity [m^2/s]
γ	Electrical conductivity [S/m]
$\mathbf{B}$	Magnetic flux density [T]
$\mathbf{E}$	Electric field intensity [N/C] or [V/m]
$\mathbf{F}$	Force [N]
$\mathbf{J}$	Volume current density $[A/m^2]$
$\mathbf{r}$	Position vector [m]
$\mathbf{v}$	Velocity [m/s]
Bi	Biot number [-]
Nu	Nusselt number [-]
μ	Magnetic permeability [N/A^2]
μ_0	Magnetic permeability of free space $[N/A^2]$
ω	Angular frequency
$\wr$	Separation vector [m]
ρ	Density [kg/m]
ρ	Electric charge density $[C/m^3]$
σ	Stefan-Boltzman constant [W/m^2K^4]
ε	Emissivity [-]
$\sim$	Phasor
A	Vector potential [Wb/m]
a	Current loop radius [m]

b	Current loop radius [m]
C_p	Specific heat [kJ/kg·K]
D	Diameter [m]
d	Distance between current loops [m]
$E(k)$	Complete elliptic integral of the first kind [-]
h	Heat transfer coefficient [W/(m^2·K)]
j	Complex variable $j = \sqrt{-1}$
k	Thermal conductivity [W/(m·K)]
$K(k)$	Complete elliptic integral of the second kind [-]
L_c	Characteristic length [m]
M_{ij}	Mutual inductance between current loops i and j
P	Power [W]
q	Charge [C]
R	Radius [m]
S	Area [m^2]
T	Temperature [K]
t	Time [s]
V	Volume [m^3]
ELM	Electromagnetic Levitation Melting
EM	Electromagnetic
FEM	Finite Element Method
FVM	Finite Volume Method

Chapter 1

Introduction

The processes taking place inside high temperature industrial operations will influence the quality of the product that is produced and how frequently maintenance is required on the plant. For example, Figure 1.1 shows a simplified schematic of a furnace where the fluid flow and heat transfer of the molten metal and slag inside the furnace will determine the quality of the metal produced by the furnace and the furnace operation time before it will be necessary to do maintenance work. An understanding of the heat transfer and fluid flow processes taking place inside this furnace will therefore be valuable.

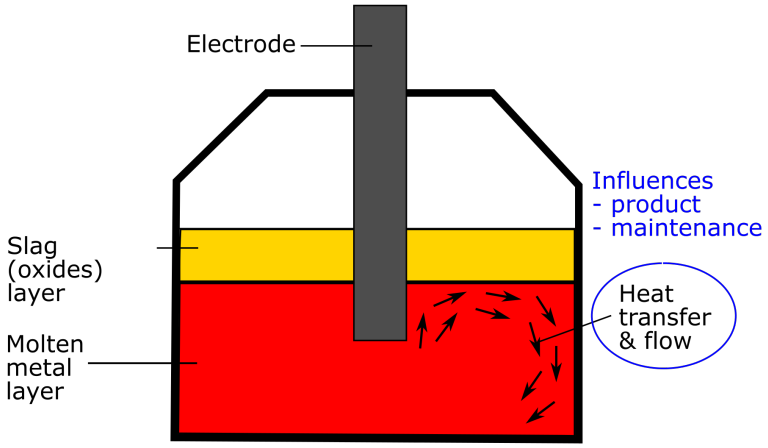

Figure 1.1: Simplified schematic of an industrial furnace.

High temperatures and a chemically aggressive environment makes it difficult to do experimental investigations around high temperature industrial processes, for example the melting and smelting processes taking place inside furnaces. Fortunately mathematical models can be used in conjunction with the limited experimental results that are available to increase our understanding of these high temperature processes. However, mathematical models of high temperature processes require

high temperature material properties. These are difficult to measure experimentally since sample contamination often occurs at these high temperatures. Figure 1.2 shows examples of contamination that occurred during high temperature experiments done at the University of Pretoria.

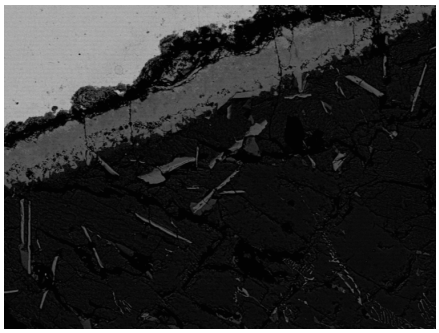

(a) Vanadium oxide sample in an iron crucible (SEM image).

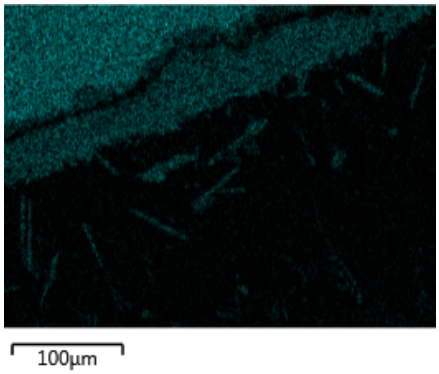

(b) Vanadium oxide sample in an iron crucible (SEM) with iron highlighted in blue.

(c) Crucible after use in experiments with vanadium at 600°C.

Figure 1.2: Examples of sample contamination during high temperature experiments performed at the University of Pretoria.

Figure 1.2a shows a scanning electron microscope (SEM) image of the edge of a iron crucible containing a vanadium sample. The same image is repeated in Figure 1.2b with all the iron in the image highlighted in blue to show how the iron con-

taminates the vanadium (black, middle and bottom of the image). In Figure 1.2c contamination of a crucible that was used for vanadium experiments at 600°C can be seen.

The melting point of some materials are so high that it is not always possible to obtain container materials that can withstand high enough temperatures to investigate these materials during melting. One possible solution to overcome the difficulties of sample contamination and materials with high melting temperatures, is to make use of electromagnetic levitation melting. Electromagnetic levitation melting (ELM) was patented in 1925 by Otto Muck [11] and is a containerless processing technique that allows for the characterisation of high temperature material properties. Other applications of levitation melting include the positioning of samples during processing experiments conducted in microgravity in space [4], studies of the melting and freezing phenomena of metallic liquids [14], and the synthesis and manipulation of nanoparticles [8].

An electromagnetic levitation cell consists of a generally conically wound, water cooled copper tube which carries a large, high frequency alternating current. Typical electrical current values reported in literature for use in levitation cell experiments are 400 A alternating at a frequency of 450 Hz [4], 500 A at 270 Hz [6], and 170 A at 178 Hz. As there is always an associated magnetic field around a current carrying conductor, an alternating magnetic field will be created around the coil loops. If a sample of an electrically conductive material is placed inside the coil, the alternating magnetic field will induce eddy currents inside the sample according to Faraday's law. The sense of magnetic field associated with these eddy currents will be such that it opposes the magnetic field of the coil and generates a Lorentz force that levitates the sample. Additionally, the eddy current is also responsible for the Ohmic heating and melting of the sample while it is levitated. The electromagnetic levitation cell shown in Figure 1.3 was built at the University of Pretoria and it could potentially be utilised for this purpose.

(a) Levitation cell.

(b) Detail of levitation cell coil.

Figure 1.3: The electromagnetic levitation cell at the University of Pretoria.

Figure 1.4 shows an aluminium sample being melted and heated while levitated in the electromagnetic levitation cell at the University of Pretoria.

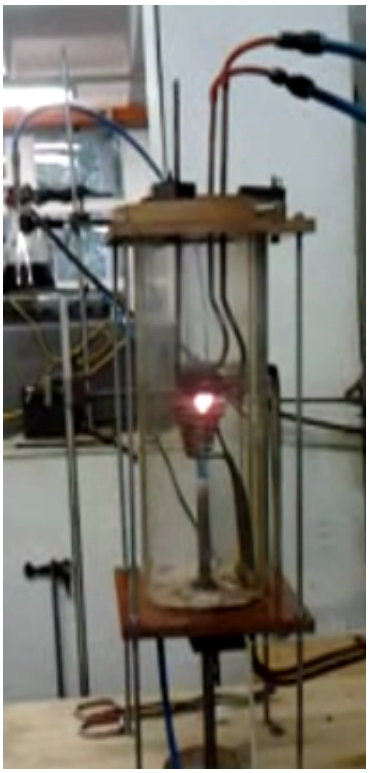

(a) Levitation cell in operation.

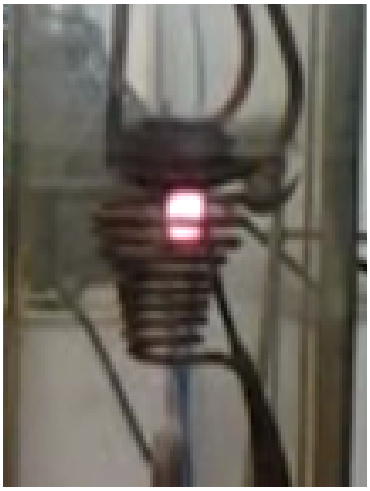

(b) Levitation melting of an aluminium sample.

Figure 1.4: Levitation melting of an aluminium sample with the electromagnetic levitation cell at the University of Pretoria.

The behaviour of electromagnetic levitation cells is complicated by the fact that changes in coil design, sample size and sample material all affect the levitation force and sample temperature, and these interactions are not yet well understood. This especially becomes a challenge when attempting to design levitation experiments. In this context mathematical models are a useful tools to better understand and predict levitation cell behaviour. The first levitation cell model was developed in 1952 when Okress et al. [12] undertook an experimental investigation of levitation melting and presented a simplified analytical model of the levitation cell to prove the principle of levitation melting.

In this work a numerical model of an electromagnetic levitation cell is implemented and used to investigate the behaviour of the levitation cell and the sensitivity of levitation cell operation to variations in coil design, sample material and sample size. A description of the mathematical background of the model is given in chapter 2 and some details on the model implementation are given in chapter 3. The process that is followed to verify and validate the model is reported in chapter 4. The model is used in an investigation to determine the effect that changes in the coil current and lid height have on the sample position and temperature and these results are reported in chapter 5.

Chapter 2

Model Description

2.1 Introduction

The design of an electromagnetic levitation cell influences the sample weight that can be levitated as well as the temperature the sample will be heated to. Knowledge about the accessible sample weight and temperature ranges with a specific levitation cell will make it easier to use the levitation cell productively for high temperature material property measurements. Therefore, a numerical electromagnetic levitation cell model will be useful to support experimental work. A model will further allow the design of levitation cells for heating specified sample materials to specified temperatures.

The levitation cell model requires the user to supply information about the coil geometry, coil current, sample size, sample material properties, and the material properties of the atmosphere around the sample. The model then computes whether or not the sample can be levitated, in which position inside the coil the sample will be levitated, whether this levitation position is stable, and to what steady state temperature the sample will be heated in this position.

A levitation cell model broadly consists of two parts: first an electromagnetic part is required to find the levitation force and the power absorbed in the sample, and then a heat transfer calculation determines the sample temperature. The model could also include a third part where the deformation and oscillation of the sample is computed, but this is excluded from the scope of the current modelling work.

This chapter gives a short overview of the different approaches to levitation cell modelling in literature. The choice of modelling approach for the current application is then motivated and a description with some background of the model is given.

2.2 Electromagnetic model

2.2.1 Electromagnetic model literature

Overall the levitation cell model should be able to predict both the levitation force acting on the sample and the sample temperature. In the electromagnetic part of the model, this requires the calculation of the power absorbed by the sample from the induced current density in the sample. In addition we need to find the magnetic flux density in the sample for the calculation of the levitation force. El-Kaddah and Szekely [4] point out that there are two different approaches that can be followed to obtain the induced current density and magnetic flux density:

1. the **mutual inductance approach** makes use of the concept of mutual inductance to compute the induced current in the sample. Once the induced current is known, the magnetic flux density can then be calculated, or
2. the partial differential Maxwell's equations can be solved over the entire domain to find the magnetic flux density field and hence the induced current can be computed. This approach will further be referred to as the **magnetic flux density approach**.

A variety of levitation cell models exist in literature. Which one of the two approaches above is followed is one of the main differences between models; together with the method used to solve the partial differential equations and the simplifying assumptions in the model. A number of the levitation cell models in literature are now reviewed in order to choose an appropriate modelling approach for this investigation. Tables 2.1 and 2.2 give a comparative summary of the reviewed models. A simplifying assumption common to all the reviewed models is that the helical coil is approximated by a set of circular loops resulting in a rotationally symmetric geometry and thus reducing a three-dimensional solution domain to a two-dimensional one.

Mutual inductance approach

The models listed in Table 2.1 follow the first approach, using the principle of mutual inductance to find the induced current before computing the magnetic flux density from the result. All the models discussed here make use of constant material property values throughout the domain and do not account for changes in property values with changes in temperature.

The levitation cell model proposed by Okress et al. [12] in 1952 is a simplified analytical model. It was developed to illustrate the principle of electromagnetic levitation melting assuming a spherical, homogeneous metal sample in a levitation coil consisting of only one or two coil loops. The model assumes that the magnetic field is uniform across the sample and is therefore only accurate for samples small enough with respect to the coil for this assumption to be reasonable. The model approximates the eddy currents on the surface of the sample with a single current

on the equator of the sample. The mutual inductance between this single current on the equator of the sample and the coil is used to compute the induced current in the sample. Okress et al. [12] are able to experimentally validate their model for small samples with diameters of about 20% of the coil loop diameter, but report that validation was less successful for larger samples with diameters of about 30% of the coil loop diameter.

In 1965 Fromm and Jehn [6] extended the model of Okress et al. to include multi-loop, arbitrary coil geometries, but only validate their extended model for the case of a single loop coil. Fromm and Jehn [6] found good agreement between their model and experimental results from a single-loop coil.

Recently, in 2013, Royer et al. [14] used a modified version of the model of Fromm and Jehn [6] with a genetic-like optimization algorithm to design levitation cells. Just like Fromm and Jehn and Okress et al., Royer et al. approximate the induced current with a single current loop on the equator of the sample and then use the result to compute the power absorbed by the sample. However, in an attempt to account for the fact that the actual absorbed power across the sample is not uniformly distributed, Royer et al. [14] discretize the sample in horizontal slices and modify the absorbed power by taking a volume weighted average of the original value.

In 1983 and 2006 respectively, El-Kaddah and Szekely [4] and Moghimi et al. [10] developed models using the principle of mutual inductance in finite volume method (FVM) formulations. The sample is still assumed to be spherical, but because these are distributed parameter models, the assumption of a uniform magnetic field across the sample is not necessary. This means that the model can now be used with samples of any size - not just samples that are small with respect to the coil. The sample is discretized into a set of adjacent rings and then the mutual inductance between the sample rings and coil rings is used to compute the induced current density field in the sample.

Moghimi et al. [10] divide the sample into a set of horizontal disk-shaped slices where each slice consists of a number of rings. El-Kaddah and Szekely [4] model the sample as a number of concentric spherical shells which are again divided into various segments of constant current density. El-Kaddah and Szekely [4] find that the sample temperature predicted by the model is similar to the experimentally obtained temperature. However in order to do this comparison the magnitude of the electrical current in the coil during the experiment could not be measured independently and it is deduced from the heat transfer calculation. Moghimi et al. [10] compared their model results to experimental measurements of the sample temperature for various input power settings and found good agreement for the power settings larger than 75% of 15 kW.

Table 2.1: Levitation cell models in literature using the principle of mutual inductance to find the current induced in the sample.

	Okress et al. [12]	Fromm & Jehn [6]	El-Kaddah & Szekely [4]	Moghimi et al. [10]	Royer et al. [14]
Year published	1952	1965	1983	2006	2013
Model type	Simplified analytical lumped parameter model. Aiming just to illustrate the principle of ELM.	Extended version of simplified analytical lumped parameter model of Okress et al. [12].	Own implementation of the Finite Volume Method.	Own implementation of the Finite Volume Method.	The model of Fromm & Jehn [6] with modifications in the induced power calculation.
Number of coil loops	One or two	Multiple	Multiple	Multiple	Multiple
Sample shape and size	Spherical, small with respect to the coil	Spherical, small with respect to the coil	Spherical, any size	Spherical, any size	Spherical, small with respect to the coil
Assumptions about the sample material	Homogeneous metal	Homogeneous metal	Non-ferromagnetic	Non-ferromagnetic	Homogeneous metal
Assuming a uniform magnetic field in the sample	Yes	Yes	No	No	Yes
Temperature dependent material properties	No	No	No	No	No
Verification / Validation	Levitation force validated for a small sample in a single loop coil. Good agreement when sample diameter is $\leq$ 20% of the coil loop diameter.	Levitation force validated for single loop coils only.	Partial validation of the sample temperature.	Partial validation of the sample temperature.	Levitation force validated for single loop coils only, partial validation of the sample temperature.

Magnetic flux density approach

The models listed in Table 2.2 first solve for the magnetic flux density by solving Maxwell's partial differential equations for a domain that includes both the sample and the levitation cell coil. Since this approach starts with finding the magnetic flux density field, none of these models assume a uniform magnetic field across the sample and consequently there is no assumption that limits sample sizes. All these models are developed for non-ferromagnetic metal samples levitated in multi-loop levitation cell coils.

Lohöfer [9] describes an analytical solution for the power absorbed by a spherical sample in a levitation cell. The model does not include variation of material property values with changes in temperature and is not validated against experimental results.

Kermanpur et al. [8] develop a coupled-field electromagnetic-thermal model for electromagnetic levitation melting of metals using a finite element formulation in the commercial software package ANSYS. They take the temperature dependence of the material properties in the levitation cell model into account through an iterative procedure. Kermanpur et al. [8] first assume a sample temperature and do an alternating current (AC) harmonic analysis of Maxwell's equations, followed by a thermal analysis to determine the sample temperature, all while assuming constant material properties. If the sample temperature differs significantly from the assumed temperature, it is updated and the full electromagnetic and thermal computations are repeated until the sample temperature converges. Kermanpur et al. [8] are able to verify their model results against the model results of Moghimi et al. [10].

Feng and Shi [5] present a levitation cell model using an Arbitrary Lagrangian-Eularian (ALE) finite element method. This allows modelling of any sample shape as well as the deformation of the sample. The model of Feng and Shi [5] assumes temperature independent material property values. Feng and Shi [5] validate the lifting force predicted by their model against experimental results from literature and the power absorbed by the sample against an analytical model.

Table 2.2: Levitation cell models in literature solving for the magnetic flux density over the entire domain.

	Lohöfer [9]	Kermanpur et al. [8]	Feng & Shi [5]
Year published	1989	2011	2016
Model type	Analytical solution of partial differential equations	Coupled field EM-thermal FEM built in ANSYS	Abitrary Lagrangian-Eulerian FE model
Number of coil loops	Multiple	Multiple	Multiple
Sample shape and size	Spherical, any size	Spherical, any size	Any shape, any size
Assumptions about the sample material	Non-ferromagnetic metal	Non-ferromagnetic metal	Non-ferromagnetic metal
Assuming a uniform magnetic field in the sample	No	No	No
Temperature dependent material properties	No	Yes	No
Verification / Validation	No	Validation against the model of Moghimi et al. [10]	Lifting force validated against experimental results from literature; absorbed power validated against analytical model results from literature

2.2.2 Electromagnetic model decision

A model used for the design of electromagnetic levitation cells must have the ability to evaluate a wide variety of sample sizes and coil designs. Models like those used by Okress et al. [12], Fromm and Jehn [6] and Royer et al. [14] are not ideal for this application, because they rely on a small sample assumption and are therefore only accurate for a limited range of sample sizes. An implementation of this kind of model would limit the designs that can be considered to only those within a limited range of coil to sample diameter ratios. The model of Lohöfer [9] is also not adequate because it only describes the power absorbed by the sample and not the levitation force acting on the sample. This model would therefore not be able to predict what sample sizes could be levitated by a certain coil design. It is therefore decided to follow the approach of El-Kaddah and Szekely [4] and Moghimi et al. [10] and implement a finite volume method model of the levitation cell using the principle of mutual inductance.

2.2.3 Theoretical framework of the electromagnetic model

This section describes the theoretical background for the electromagnetic part of the finite volume levitation cell model. The section starts with background on Maxwell's equations, which are the governing equations that are solved in the electromagnetic model. The implemented electromagnetic model is then derived from Maxwell's equations.

Electromagnetism: background and Maxwell's equations

Electromagnetism or electrodynamics is a branch of classical mechanics that deals with electromagnetic fields and the charged particles required to create these fields [7]. Mechanics is generally concerned with the reaction of a system under the influence of a force. In electrodynamics this force is the electromagnetic force.

Maxwell's equations are a set of four partial differential equations that describe electrodynamics when viewed in conjunction with the force law [7]. In its most general form, Maxwell's equations with their names are [7]:

$$\nabla \cdot \mathbf{E} = \frac{1}{\epsilon_0}\rho \qquad \text{(Gauss' law)} \qquad (2.1a)$$

$$\nabla \cdot \mathbf{B} = 0 \qquad \text{(no name)} \qquad (2.1b)$$

$$\nabla \times \mathbf{E} = -\frac{\partial \mathbf{B}}{\partial t} \qquad \text{(Faraday's law)} \qquad (2.1c)$$

$$\nabla \times \mathbf{B} = \mu_0 \mathbf{J} + \mu_0 \epsilon_0 \frac{\partial \mathbf{E}}{\partial t} \qquad \text{(Ampére's law with Maxwell's correction)} . \qquad (2.1d)$$

Equation (2.1a) is Gauss' law which states that an electric field $\mathbf{E}$ is a consequence of electric charge [7]. In this equation electric charge is represented by the electric

charge densityρ . $\epsilon_0 = 8.85 \times 10^{12}$ C^2/Nm^2 is the electric constant, also called the permittivity of free space.

Equation (2.1b) is unnamed and states that the magnetic flux density field **B** is divergenceless [7]. A divergenceless field is a field without any point sources. Therefore magnetic field lines do not start or end at a point, but rather form closed loops.

Faraday's law is given in equation (2.1c) and states that a time-varying magnetic field induces an electric field.

Ampére's law with Maxwell's correction, given in equation (2.1d), states that magnetic fields exist as a result of electric current or as a result of time-varying electric fields [7]. In this equation **J** denotes the volume current density and the constant $\mu_0 = 4\pi \times 10^{-7}$N/A^2 is the magnetic permeability of free space. The last term in equation (2.1d) is known as the displacement current term.

The Lorentz force law is given by:

$$\mathbf{F} = q(\mathbf{E} + \mathbf{v} \times \mathbf{B}) \tag{2.2}$$

where **F** denotes force and q is a charge moving with velocity v. The force law describes how electromagnetic fields are influenced by charges, while Maxwell's equations describe how charges and electric currents produce all electromagnetic fields [7, §7.3.3].

Modelling the levitation force in an electromagnetic levitation cell requires finding a way to solve for the magnetic flux density field **B** and electric field **E** in equation (2.1), and computing the Lorentz force responsible for the levitation from equation (2.2).

Model derivation

The finite volume method modelling approach of El-Kaddah and Szekely [4] is followed here. This model assumes that the helical induction coil can be approximated by an axisymmetrical set of circular loops. Figure 2.1a shows a cross-section of a coil represented by an axisymmetrical set of loops, including a levitated sample. Further, it is assumed the that the eddy currents in the sample flow in circular loops around the same axis as the current flowing in the coil loops. The sample is therefore discretized into a set of adjacent circular current carrying rings, each carrying a constant cross-sectional current density. Figure 2.1b shows the discretized sample as well as the symbols used to indicate the relative direction of the electrical current flowing in the coil loops. Figure 2.1c shows only the symbols describing the same coil design and discretized sample. From here on these symbols (or only one half, due to symmetry) will be used to illustrate coil designs. The definition of both the spherical and Cartesian coordinate systems used in the model are given in Figure 2.1a.

According to the method of El-Kaddah and Szekely [4], Faraday's law (equation (2.1c)) is written in terms of the mutual inductance between the coil rings and

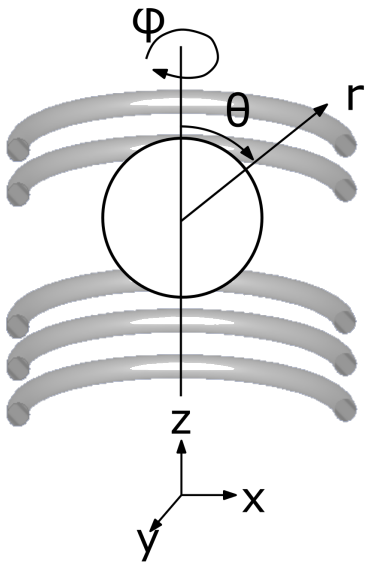

(a) Cross-section of a coil and sample with the spherical and Cartesian coordinate systems.

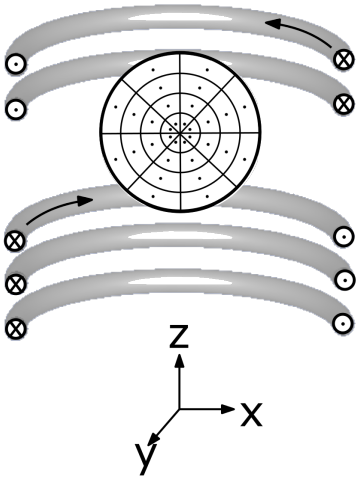

(b) Discretized sample and symbols to represent relative current direction in the coil.

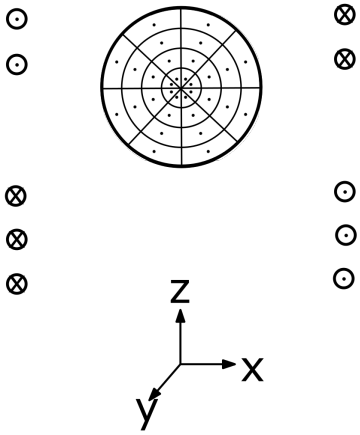

(c) Symbols used to represent the coil and sample.

Figure 2.1: Representation of the discretized axisymmetric sample and coil geometry.

discretized sample rings. The resulting linear system of equations is solved to obtain the induced current in the discretized sample rings. Once the current in the sample is known, the magnetic field is computed from Ampere's law (equation (2.1d)). The current density field inside the sample is required to compute the power absorbed by the sample and both the current density and magnetic flux fields are necessary to compute the Lorentz force acting on the sample.

El-Kaddah and Szekely [4] state that they use Faraday's law with the definition of mutual induction and phasor notation to arrive at the linear system of equations for the eddy currents in the sample. In order to recover all the assumptions made in this process and to define consistent notation, the derivation of the linear system from Faraday's law is presented here.

In equation (2.1c) Faraday's law gives the electric field induced by a time-varying magnetic field. Faraday's law can be written in integral form as [4, 7]

$$\oint_P \mathbf{E} \cdot d\mathbf{l} = -\frac{d}{dt} \int_S \mathbf{B} \cdot d\mathbf{s} \tag{2.3}$$

where $\mathbf{l}$ is an infinitesimal displacement vector along the perimeter P and $\mathbf{s}$ is an infinitesimal surface element on surface S.

Ohm's law states that the electric field is proportional to the current density field, where the proportionality factor is the electrical conductivity of the medium, γ [7, §7.1.1]

$$\mathbf{J} = \gamma \mathbf{E} \, . \tag{2.4}$$

Using Ohm's law and assuming that the electrical conductivity of each discretized sample loop is constant, the left-hand side of equation (2.3) is rewritten in terms of current density

$$\frac{1}{\gamma} \oint_P \mathbf{J} \cdot d\mathbf{l} = -\frac{d}{dt} \int_S \mathbf{B} \cdot d\mathbf{s} \tag{2.5}$$

From differential calculus it is known that the divergence of the curl of a vector is always zero [7, §1.2.7], e.g. for the arbitrary vector $\mathbf{F}$,

$$\nabla \cdot (\nabla \times \mathbf{F}) = 0. \tag{2.6}$$

A divergenceless vector can therefore be replaced with the curl of a different vector. Recall from equation (2.1b) in Maxwell's equations that the magnetic flux density is divergenceless

$$\nabla \cdot \mathbf{B} = 0. \tag{2.7}$$

It is therefore possible and customary in electrodynamics to define the vector potential $\mathbf{A}$, such that

$$\mathbf{B} = \nabla \times \mathbf{A} \tag{2.8}$$

and

$$\nabla \cdot (\nabla \times \mathbf{A}) = 0. \tag{2.9}$$

Substituting equation (2.8) into equation (2.5) gives

$$\frac{1}{\gamma} \oint_P \mathbf{J} \cdot d\mathbf{l} = -\frac{d}{dt} \int_S (\nabla \times \mathbf{A}) \cdot d\mathbf{s}. \tag{2.10}$$

Using Stokes' theorem, the right-hand side of equation (2.10) can be written as a closed path integral

$$\frac{1}{\gamma} \oint_P \mathbf{J} \cdot d\mathbf{l} = -\frac{d}{dt} \oint_P \mathbf{A} \cdot d\mathbf{l}. \tag{2.11}$$

The right-hand side of equation (2.11) can now be written in terms of mutual inductance by using Ampére's law, equation (2.1d).

The levitation cells described in literature operate at electrical and magnetic field frequencies of a few hundred kilohertz [4, 5, 8, 14]. At these frequencies ($< 10^6$ Hz), the electromagnetic wavelengths are much larger (> 100m) than the levitation cell (< 0.1m), and therefore the displacement current term ($\mu_0 \epsilon_0 \frac{\partial \mathbf{E}}{\partial t}$) becomes negligible [9]. Dropping the displacement current term and substituting equation (2.8) into equation (2.1d), it becomes

$$\nabla \times (\nabla \times \mathbf{A}) = \mu_0 \mathbf{J}. \tag{2.12}$$

By substituting in the curl of a curl identity [7, §1.2.7, §5.4.1] this becomes

$$\nabla (\nabla \cdot \mathbf{A}) - \nabla^2 \mathbf{A} = \mu_0 \mathbf{J}. \tag{2.13}$$

According to the Helmholtz theorem a vector field is completely uniquely determined by its divergence, curl and boundary conditions [7, §1.6.1]. The curl of the magnetic vector potential is defined in equation (2.8), but its divergence has not yet been defined. It can be shown that the divergence of $\mathbf{A}$ can be chosen as any function with no curl [7, §5.4.1]. The simplest choice is

$$\nabla \cdot \mathbf{A} = 0 \tag{2.14}$$

and this is called the Coulomb gauge [7]. Equation (2.13) now reduces to

$$\nabla^2 \mathbf{A} = -\mu_0 \mathbf{J}. \tag{2.15}$$

Equation (2.15) is three Poisson's equations, one in each Cartesian direction. The solution to Poisson's equation is known, and in this case it is given by [7, §5.4.1]

$$\mathbf{A}(\mathbf{r}) = \frac{\mu_0}{4\pi} \int \frac{\mathbf{J}(\mathbf{r}')}{\wp} \, dV' \tag{2.16}$$

where V' is the infinitesimal volume of the source point, $\mathbf{r}'$ is a source point where electric charge is located, $\mathbf{r}$ is a field point where the magnetic vector potential is evaluated, and $\wp$ is the separation vector from the source point to the field point. A field point is a point in space where the electromagnetic field is evaluated. A source point is the location of a point charge in space. The $'$-symbol is used to indicate source points. The separation vector $\boldsymbol{\wp}$ is then a vector from a source point to a field point [7]. In Figure 2.2 from Griffiths [7] the definition of the position vector $\mathbf{r}$ and the unit position vector $\hat{\mathbf{r}}$ is given on the left-hand side. The right-hand side then shows the position vectors relating to a source point and a field point and defines the separation vector between them.

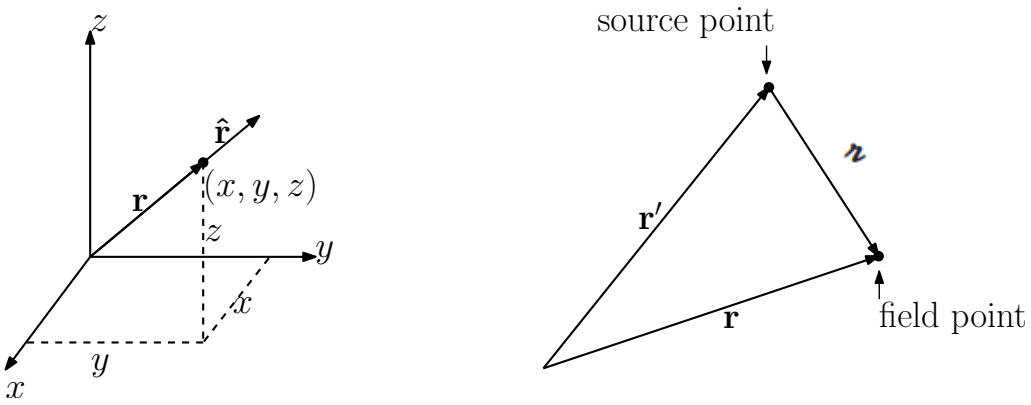

Figure 2.2: Position vectors and separation vectors (adapted from [7]).

For the purpose of the levitation cell model, a constant current density is assumed in each discretized ring. This means that the current density will be constant across the cross-sectional area of each coil and discretized sample ring, and equation (2.16) can be simplified for the case of line currents to become

$$\mathbf{A}(\mathbf{r}) = \frac{\mu_0}{4\pi} \oint_P \frac{\mathbf{J}(\mathbf{r}') S'}{\wp} \, d\mathbf{l}' \tag{2.17}$$

where S' is the cross-sectional area of the discretized ring and $d\mathbf{l}'$ is the infinitesimal displacement vector at the source point. Substituting this result into equation (2.11) gives

$$\frac{1}{\gamma}\oint_P \mathbf{J}\cdot d\mathbf{l} = -\frac{d}{dt}\oint_P \frac{\mu_0}{4\pi}\oint_P \frac{\mathbf{J}\left(\mathbf{r}'\right)S'}{\wp}\, d\mathbf{l}'\cdot d\mathbf{l} \tag{2.18}$$

where $d\mathbf{l}$ is the infinitesimal displacement vector at the field point. Assuming that the magnetic permeability μ_0, current density $\mathbf{J}\left(\mathbf{r}'\right)$, and cross-sectional area S' of each current loop is constant, this becomes

$$\frac{1}{\gamma}\oint_P \mathbf{J}\cdot d\mathbf{l} = -\frac{d}{dt}\left(\frac{\mu_0}{4\pi}\mathbf{J}\left(\mathbf{r}'\right)S'\oint_P\oint_P \frac{d\mathbf{l}'\cdot d\mathbf{l}}{\wp}\right). \tag{2.19}$$

The mutual inductance M between two current loops 1 and 2 is given by the Neumann formula [7, §7.2.3] as

$$M_{21} = \frac{\mu_0}{4\pi}\oint_P\oint_P \frac{d\mathbf{l}_1\cdot d\mathbf{l}_2}{\wp}. \tag{2.20}$$

Notice that equation (2.19) contains the expression for the mutual inductance. Equation (2.19) states that the current density at a field point is directly proportional to the mutual inductance between the field point and the source points near the field point. Choosing the field point as one of the discretized sample rings, i, and then noting that all the coil rings as well as all the discretized sample rings will act as field points, equation (2.19) can be used to write the current density in the i-th discretized sample loop in terms of the mutual inductance between a total of p coil- and discretized sample loops

$$\frac{1}{\gamma}\oint_P \mathbf{J}_i\cdot d\mathbf{l} = -\frac{d}{dt}\sum_{n=1}^{p}\left(J_n S_n M_{in}\right). \tag{2.21}$$

The constant current in a current loop can only flow in one direction along the loop, or opposite to it. Currents flowing in opposite directions are modelled with opposite signs. It is therefore no longer necessary to represent current and current density as vectors.

The current density and magnetic flux fields are generally functions of position and time, i.e. $J(x,y,z,t)$ and $B(x,y,z,t)$. However, in this case these are time harmonic fields that vary with a constant frequency. Complex numbers can be used to represent these fields as phasors that are only functions of position, $\widetilde{J}(x,y,z)$ and $\widetilde{B}(x,y,z)$. The time derivative of a phasor is $\widetilde{F}$ is given by $j\omega\widetilde{F}$ where $j=\sqrt{-1}$ is the complex variable and ω is the angular frequency of the phasor. Therefore equation (2.21) is represented in phasor notation as

$$\oint_P \widetilde{J}_i\cdot d\mathbf{l} = -j\omega\gamma\sum_{n=1}^{p}\left(\widetilde{J}_n S_n M_{in}\right). \tag{2.22}$$

The current density $\widetilde{J}$ in equation (2.22) can be split in two parts: the known current density in the coil and the unknown current density in the discretized sample loops

$$\oint_P \widetilde{J}_i \cdot d\mathbf{l} = -j\omega\gamma \left(\sum_{n=1}^{sample\ loops} \left(\widetilde{J}_n S_n M_{in} \right) + \sum_{n=1}^{coil\ loops} \left(\widetilde{J}_n S_n M_{in} \right) \right). \tag{2.23}$$

Noting that the input current in the coil is known and $\widetilde{I} = \widetilde{J} \times S$, moving all the terms containing unknowns to the left hand side of the equation and integrating for a constant current flowing along a circular path, the expression becomes

$$\widetilde{J}_i \left(2\pi r_{loop}\right) + j\omega\gamma \left(\sum_{n=1}^{sample\ loops} \left(\widetilde{J}_n S_n M_{in} \right) \right) = -j\omega\gamma \left(\sum_{n=1}^{coil\ loops} \left(\widetilde{I}_n M_{in} \right) \right) \tag{2.24}$$

where r_{loop} is the radius of the i-th discretized current loop. Equation (2.24) can be split into its real and imaginary components to avoid having to perform computations with complex numbers. The resulting equations

$$\begin{aligned} \mathrm{Re}(\widetilde{J}_i)\left(2\pi r_{loop}\right) + \omega\gamma \left(\sum_{n=1}^{sample\ loops} \mathrm{Im}(\widetilde{J}_n) S_n M_{in} \right) &= -\omega\gamma \left(\sum_{n=1}^{coil\ loops} \mathrm{Re}(\widetilde{I}_n) M_{in} \right) \\ \mathrm{Im}(\widetilde{J}_i)\left(2\pi r_{loop}\right) - \omega\gamma \left(\sum_{n=1}^{sample\ loops} \mathrm{Re}(\widetilde{J}_n) S_n M_{in} \right) &= \omega\gamma \left(\sum_{n=1}^{coil\ loops} \mathrm{Im}(\widetilde{I}_n) M_{in} \right) \end{aligned} \tag{2.25}$$

are those given by El-Kaddah and Szekely [4] for obtaining the induced current field inside the sample. For a sample discretized into k loops, equation (2.25) becomes a $2k \times 2k$ linear system of equations that is solved to find the current density $\widetilde{J}_n$ inside the sample [4]. The first half of the linear system contains the equations where the real part of the current density is unknown, and in the second half the imaginary part is the unknown. For a levitation cell made up of c coil loops and a sample discretized into k loops, the linear system of equations of equation (2.25) becomes

$$\begin{bmatrix} [\mathbf{F}] & [\mathbf{D}] \\ -[\mathbf{D}] & [\mathbf{F}] \end{bmatrix} \begin{Bmatrix} \mathrm{Re}(\widetilde{J}_1) \\ \mathrm{Re}(\widetilde{J}_2) \\ \vdots \\ \mathrm{Re}(\widetilde{J}_k) \\ \mathrm{Im}(\widetilde{J}_1) \\ \mathrm{Im}(\widetilde{J}_2) \\ \vdots \\ \mathrm{Im}(\widetilde{J}_k) \end{Bmatrix} = \begin{Bmatrix} -\gamma\omega \left(M_{1,1}\mathrm{Re}(\widetilde{I}_1) + M_{1,2}\mathrm{Re}(\widetilde{I}_2) + \ldots M_{1,c}\mathrm{Re}(\widetilde{I}_c) \right) \\ -\gamma\omega \left(M_{2,1}\mathrm{Re}(\widetilde{I}_1) + M_{2,2}\mathrm{Re}(\widetilde{I}_2) + \ldots M_{2,c}\mathrm{Re}(\widetilde{I}_c) \right) \\ \vdots \\ -\gamma\omega \left(M_{k,1}\mathrm{Re}(\widetilde{I}_1) + M_{k,2}\mathrm{Re}(\widetilde{I}_2) + \ldots M_{k,c}\mathrm{Re}(\widetilde{I}_c) \right) \\ \gamma\omega \left(M_{1,1}\mathrm{Im}(\widetilde{I}_1) + M_{1,2}\mathrm{Im}(\widetilde{I}_2) + \ldots M_{1,c}\mathrm{Im}(\widetilde{I}_c) \right) \\ \gamma\omega \left(M_{2,1}\mathrm{Im}(\widetilde{I}_1) + M_{2,2}\mathrm{Im}(\widetilde{I}_2) + \ldots M_{2,c}\mathrm{Im}(\widetilde{I}_c) \right) \\ \vdots \\ \gamma\omega \left(M_{k,1}\mathrm{Im}(\widetilde{I}_1) + M_{k,2}\mathrm{Im}(\widetilde{I}_2) + \ldots M_{k,c}\mathrm{Im}(\widetilde{I}_c) \right) \end{Bmatrix} \tag{2.26}$$

where the coefficient matrix is made up of the full and diagonal submatrices, [**F**] and [**D**]

$$[\mathbf{F}] = \begin{bmatrix} \gamma\omega(M_{1,1}S_1) & \gamma\omega(M_{1,2}S_2) & \ldots & \gamma\omega(M_{1,k}S_k) \\ \gamma\omega(M_{2,1}S_1) & \gamma\omega(M_{2,2}S_2) & \ldots & \gamma\omega(M_{2,k}S_k) \\ \vdots & \vdots & \ddots & \vdots \\ \gamma\omega(M_{k,1}S_1) & \gamma\omega(M_{k,2}S_2) & \ldots & \gamma\omega(M_{k,k}S_k) \end{bmatrix} \tag{2.27}$$

$$[\mathbf{D}] = \begin{bmatrix} 2\pi(r_{loop})_1 & 0 & \ldots & 0 \\ 0 & 2\pi(r_{loop})_2 & \ddots & \vdots \\ \vdots & \ddots & \ddots & 0 \\ 0 & \ldots & 0 & 2\pi(r_{loop})_k \end{bmatrix}. \tag{2.28}$$

Once the current density in the sample is known, it is substituted back into Ampére's law (equation (2.1d)) to find the magnetic flux density. In the case of the levitation cell, recall that the displacement current term in Ampére's law becomes negligible. Ampére's law reduces to the Biot-Savart law when taking this simplification into account. The magnetic flux in the sample is therefore calculated from the Biot-Savart law

$$\mathbf{B} = \frac{\mu_0}{4\pi} \int_V \frac{\mathbf{J} \times \hat{\boldsymbol{r}}}{|\boldsymbol{r}|^2} dV \tag{2.29}$$

where $\hat{\boldsymbol{r}}$ is a unit vector in the direction of the separation vector $\boldsymbol{r}$. This approach differs from that suggested by El-Kaddah and Szekely [4] to find the magnetic flux density. El-Kaddah and Szekely [4] propose substituting the current density back into equation (2.16) to find the vector potential field **A** and then differentiating (equation (2.8)) to obtain the magnetic flux density **B**. However, since we are only interested in the value of **B** we would rather substitute the current density directly into equation (2.1d). This reduces the problem from one with an integration step and a differentiation step, to only an integration problem. Removing the

differentiation step is also advantageous for numerical accuracy because numerical differentiation has the difficulty that round-off error begins to increase when the step size is decreased in an effort to reduce the truncation error [2].

With the current density and magnetic flux inside the sample both known, the lifting force acting on the sample and power absorbed by the sample can be computed. The magnetic part of the Lorentz force responsible for levitating the sample is given by [16, §5.2]

$$\mathbf{F} = \mathrm{Re}(\mathbf{J} \times \mathbf{B}). \tag{2.30}$$

The power P absorbed by the electrical circuits making up the discretized sample is calculated as

$$P = \mathrm{Re}\left(\mathbf{J} \cdot \mathbf{J}\right)/\gamma \ . \tag{2.31}$$

2.3 Heat transfer model

2.3.1 Heat transfer model literature

The power absorbed by the sample due to resistive heating (also referred to as Joule or Ohmic heating) is calculated in the electromagnetic model. The sample also loses heat through radiation and convection. When assuming thermal equilibrium, i.e. steady state conditions, this information can be used to find the sample temperature from an energy balance based on the first law of thermodynamics which states the principle of conservation of energy.

Literature generally follows one of two approaches in finding the sample temperature: either the whole temperature field across the sample is found from a finite element or finite volume solution of the continuity, momentum, and energy equations, or the average sample temperature is found in a lumped parameter approach.

El-Kaddah and Szekely [4] follow the first approach to find the temperature and velocity fields across the sample by using their own implementation of a finite volume approach to solve the continuity, momentum and energy equations. Kermanpur et al. [8] use an ANSYS FEM package to find the temperature distribution inside the sample, but they only consider conduction inside the sample and neglect convection. Feng and Shi [5] use the Arbitrary Lagrangian-Eulerian FEM method to find the temperature and velocity fields in the sample.

Fromm and Jehn [6] and Moghimi et al. [10] follow the second approach with a lumped parameter model and only consider radiation heat loss as their experiments are performed under vacuum. Royer et al. [14] also find the average sample temperature from a lumped parameter energy balance, considering both radiation and convection heat losses.

2.3.2 Heat transfer model decision

The Biot number, Bi, can be used to evaluate whether is it reasonable to use a lumped parameter analysis to approximate heat transfer between a solid body and the surrounding fluid [3, §4.1]. The Biot number is essentially the ratio between the convection heat transfer around the body and the conduction inside the body, and is given by

$$\mathrm{Bi} = \frac{hL_c}{k} \tag{2.32}$$

where h is the convective heat transfer coefficient between the body and the surrounding fluid, $L_c = V/S$ is the characteristic length of the body given by the ratio between its volume and surface area, and k is the thermal conductivity of the body. If the Biot number is small it means that the conduction heat transfer inside the body is more prominent relative to the convection heat transfer on the surface of the body. This results in small temperature gradients inside the body which makes the lumped parameter approach a reasonable assumption. A lumped parameter model is generally considered applicable [3] for

$$\mathrm{Bi} \leq 0.1. \tag{2.33}$$

When considering a sample inside the levitation cell, the worst-case scenario for the lumped parameter approach would be a large sample, a large convective heat transfer coefficient and a sample material with a small thermal conductivity. Samples used with the levitation cell are usually assumed to be spherical and have diameters of around 1 cm. Therefore a large sample could have a diameter D of 2.5 cm. In mass terms this is equivalent to a 73 g copper sample, a 22 g aluminium sample, or a 64 g iron sample. A sample with $D = 2.5$ cm has a characteristic length of

$$L_c = \frac{V}{S} = \frac{(1/6)\pi D^3}{\pi D^2} = \frac{1}{6}D = \frac{1}{6}(0.025) = 0.004 \text{ m}. \tag{2.34}$$

The convective heat transfer coefficient for forced convection of gases is typically between 25 W/m^2 K and 250 W/m^2 K [3, §1.7, Table 1.5]. The thermal conductivities of metals at 300 K typically varies between 12 W/mK for stainless steel, and 401 W/mK for pure copper [3, Table A-3]. The sample is heated in the levitation cell and therefore its temperature will be higher than 300 K. However, thermal conductivity increases with temperature according to the Wiedemann-Franz law [18]. The thermal conductivity at a low temperature can therefore be used for a worst-case scenario calculation, because the higher thermal conductivity value at higher temperatures will only make the lumped parameter model more valid. Using these values, the Biot number for the most unfavourable state of the levitation cell for lumped parameter modeling becomes

$$\mathrm{Bi} = \frac{hL_c}{k} = \frac{(250)(0.004)}{12} = 0.083 \leq 0.1. \tag{2.35}$$

A lumped parameter model is therefore a reasonable approximation for heat transfer from a levitated sample in a levitation cell. This is further supported by the small temperature gradients found inside the sample by El-Kaddah and Szekely [4] and Feng and Shi [5]. The model of El-Kaddah and Szekely [4] predicted that the temperature of an iron sample would vary between 1642°C in the center and 1649°C on the surface of the sample. Feng and Shi [5] only found predicted temperature variations between 901.22K and 901.3 K from the center to the surface of a levitated silver sample. The temperature variation within the sample is therefore expected to be small relative to the temperature difference between the sample and the surroundings and a lumped parameter approach is justified. It is decided to follow the approach of Fromm and Jehn [6], Moghimi et al. [10] and Royer et al. [14] and implement a lumped parameter heat transfer model.

2.3.3 Heat transfer model implementation

Assuming thermal equilibrium or steady state conditions, the heat transfer rate $\dot{Q}$ into the sample should be the same as the heat transfer out of the sample

$$\dot{Q}_{in} = \dot{Q}_{out}. \tag{2.36}$$

For the case of the levitated sample this means that the power P absorbed by the sample due to Ohmic heating must be equal to the radiation and convection heat losses

$$\begin{aligned} P &= \dot{Q}_{rad} + \dot{Q}_{conv} \\ P &= \left[\sigma\varepsilon S(T^4 - T_0^4)\right] + \left[hS(T - T_s)\right] \end{aligned} \tag{2.37}$$

where σ is the Stefan-Boltzman constant, ε is the emissivity of the sample, and T is temperature. The heat transfer coefficient h in equation (2.37) is estimated in terms of the Nusselt number, Nu, as

$$h = \frac{k}{2R}\mathrm{Nu} \tag{2.38}$$

where the Nusselt number for a sphere is given by [14]

$$\mathrm{Nu} = 2 + 0.6\left(2Rv_\infty\frac{\rho}{\eta}\right)^{1/2}\left(C_p\frac{\eta}{k}\right). \tag{2.39}$$

R is the radius of the sphere, v_∞ is the freestream velocity, ρ is the density, η is the kinematic viscosity, and C_p is the specific heat of the fluid. The sample temperature is given implicitly in equation (2.37). Therefore, the sample temperature is found upon convergence of the Newton-Raphson method

$$T_{n+1} = T_n - \frac{\mathcal{R}(T_n)}{\mathcal{R}'(T_n)} \tag{2.40}$$

where the residual is defined from equation (2.37) as

$$\mathcal{R} = P - \left[\sigma\varepsilon S(T^4 - T_0^4)\right] - \left[hS(T - T_s)\right] \tag{2.41}$$

and its derivative with respect to temperature is

$$\mathcal{R}'(T) = \frac{dR}{dT} = 0 - 4\sigma\varepsilon S T^3 - hS. \tag{2.42}$$

2.4 Summary of levitation cell model assumptions

We implement a levitation cell model where the electrodynamic problem is solved using a finite volume formulation based on the principle of mutual inductance. A distributed parameter electromagnetic model is implemented to avoid limitations on the sample size that can be modelled. The finite volume model is simplified by assuming that the sample and the levitation cell coil are rotationally symmetric around the z-axis. This requires the helical coil to be approximated by a set of circular loops, as well as the assumption that the currents induced in the sample only flow along the direction of these circular loops. At the operating frequencies of the levitation cell, the displacement current term in Ampére's law becomes negligible for objects of the levitation cell's size and therefore a quasi-static assumption is made where the displacement current term is neglected. In this part of the model the levitation force and power absorbed by the sample due to ohmic heating is calculated.

The sample temperature is calculated by the heat transfer part of the model. Here the temperature gradient across the sample is assumed to be small enough to justify a lumped parameter approach.

Chapter 3

Model Implementation

3.1 Introduction and program structure

Implementation of the mathematical model described in Chapter 2 mainly requires numerically solving equations (2.26) and (2.29) to find the current density and magnetic flux density fields in the electromagnetic part of the problem, and then solving for the sample temperature from equation (2.41). We write a Python program to solve these equations. Python 3.4 is used to develop the program with extensive use of the NumPy package for accessing mathematical functions and speeding up calculations with vectorization using NumPy arrays. The PyLab package in Python is used to plot the model output and results. The flow chart in Figure 3.1 gives the structure of the implemented Python program for modelling electromagnetic levitation cells.

The levitation cell model consists of four parts: reading input from the user, an electromagnetic model, a heat transfer model and returning the output of the model computations to the user. These four parts are indicated by the grey blocks on the left hand side of the flow chart (Figure 3.1) and this chapter deals with their numerical implementation in Python. It can be seen from the flow chart that the majority of the computations done by the levitation cell model happens in the electromagnetic part. This includes sample discretization, solution of the linear system given in equation (2.26) to find the induced current, magnetic flux computation according to equation (2.29) and ultimately computation of the levitation force and absorbed power from these results.

Our model implementation is based on the model proposed by El-Kaddah and Szekely [4] but differs mainly in how the magnetic flux density is computed, and the use of a lumped parameter approach for the heat transfer part of the model. This chapter explains the details of our model implementation that are not described by, or differ from the model proposed by El-Kaddah and Szekely [4].

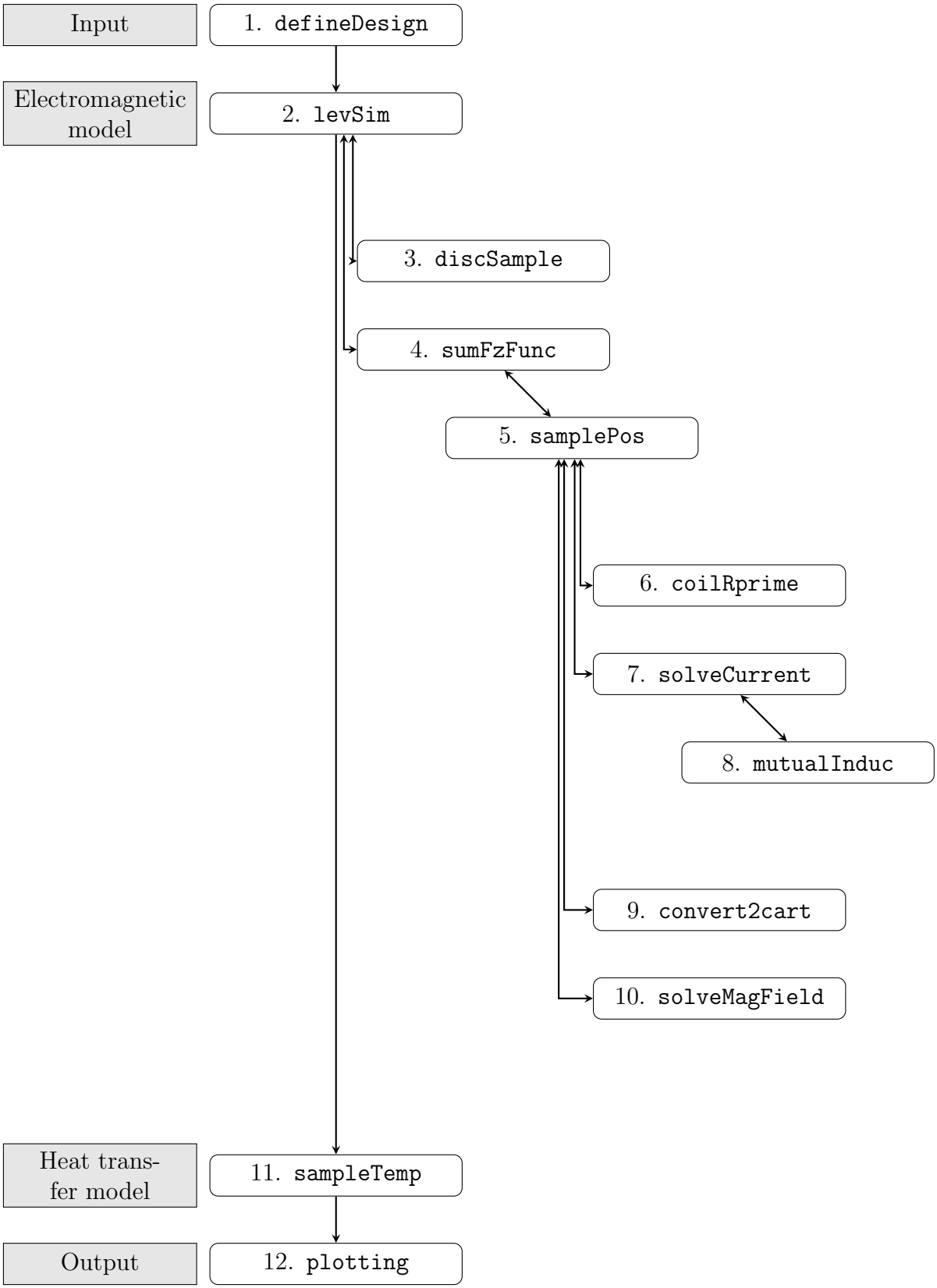

Figure 3.1: Program structure of the implemented levitation cell model.

3.2 Input structure

The levitation cell model requires information about the coil geometry as well as the material properties of the sample and the atmosphere in which it is levitated. Although procedural rather than object orientated programming is used to build the model, Python objects are created in the `defineDesign` script (block number 1 on the flow chart in Figure 3.1) and used to save this information about the coil, sample and atmosphere. These objects only have attributes and no methods, effectively making them similar to structures in other programming languages. The properties and their units that are saved as attributes of each of the three objects are given in Table 3.1.

Table 3.1: Properties of the coil, sample and atmosphere input data structures saved as attributes of objects in the levitation cell model.

Coil	Sample	Atmosphere
NumPy array of coil loop radii, x_i [m]	Emissivity, ε [-]	Fluid temperature, T_s [K]
NumPy array of coil loop heights, z_i [m]	Electrical conductivity, γ [S/m]	Environment temperature, T_0 [K]
Binary NumPy array indicating coil loop current direction, k_i [-]	Magnetic permeability, μ [H/m]	Thermal conductivity, k [W/mK]
Coil current magnitude, I [A]	Sample radius, R [m]	Fluid velocity, v [m/s]
Coil current frequency, f [Hz]	Sample density, ρ [kg/m^3]	Fluid density, ρ [kg/m^3]
Coil tube radius, r_{tube} [m]	Melting point, T_m [K]	Kinematic viscosity, ν [m^2/s]
		Specific heat, C_p [J/kgK]

An advantage of using objects to store the input data is that different samples, atmospheres or coil designs can easily be defined as new instances of the sample, coil and atmosphere objects. Further, the `levSim` function (block number 2 in the flow chart) takes the coil, sample and atmosphere objects in as arguments. Calling the `levSim` function with different instances of the coil, sample and atmosphere as arguments allows for easy comparison of different possible experimental scenarios.

3.3 Discretization

3.3.1 Spherical and rectangular coordinate systems

We choose to implement a finite volume electromagnetic model and therefore the first step in the electromagnetic model is to discretize the solution domain. The

magnetic flux density and current density fields inside the sample are required outputs of the electromagnetic model. The solution domain is therefore the spherical sample, but due to the assumption that the levitation cell is rotational symmetric, it is only necessary to find the field values on one half-circular axisymmetric plane. However, the whole three dimensional sample still has to be discretized to enable the computation of the separation vectors that will be discussed in Section 3.5.1.

The `discSample` function of block number three in Figure 3.1 discretizes a spherical sample. The sample is discretized in the spherical coordinate system as proposed by El-Kaddah and Szekely [4]. The definitions of both the spherical and Cartesian coordinate systems used in the model are given in Figure 2.1a. In the radial direction the spherical sample is divided into a number of concentric spherical shells of equal skin thickness. Along the θ-direction the spherical sample is divided into cells with different inclinations. In the ϕ-direction the sample is divided into a number of spherical wedges. The coordinates of the center point of each cell is then saved in a matrix with columns for the ρ-coordinate, θ-coordinate, ϕ-coordinate, cell area on the symmetry plane and cell volume. As the model computations and especially the cross products are simpler to perform using the Cartesian coordinate system, the coordinates of the cell center points are also converted to the Cartesian coordinate system. The Cartesian coordinate discretization is saved in a similar matrix with columns containing the x-, y-, z-coordinates of the cell center, and axisymmetric cross-sectional area of the cell.

Meshing for the skin effect

Zong et al. [19] point out that large gradients occur within the skin of the sample due to the skin effect and that this can cause numerical instabilities in distributed parameter models with an insufficient number of cells in this area. The skin effect is the phenomena of alternating currents to only penetrate a small depth of a conductor and damp out towards the center of the conductor [1]. The skin depth decreases with increasing alternating current frequency.

In the mesh described above the sample was discretized into a number of shells of equal thickness in the radial direction. In order to increase the number of cells within the skin of the sample the equal spacing of the shell radii is squared (or raised to the third or fourth power) and normalized back to fit into the sample radius. This results in a mesh with many cells close to the sample surface and fewer cells in the center of the sample where we do not expect large gradients.

3.4 Induced current computation

The computation of the induced current in the sample is done by the `solveCurrent` function in Figure 3.1. Finding the induced current field just requires setting up and solving the linear system of equations given in equation (2.26) as proposed by El-Kaddah and Szekely [4], and derived in Chapter 2. The linear system is repeated

here for easy reference

$$\begin{bmatrix} [\mathbf{F}] & [\mathbf{D}] \\ -[\mathbf{D}] & [\mathbf{F}] \end{bmatrix} \begin{Bmatrix} \mathrm{Re}(\widetilde{J}_1) \\ \mathrm{Re}(\widetilde{J}_2) \\ \vdots \\ \mathrm{Re}(\widetilde{J}_k) \\ \mathrm{Im}(\widetilde{J}_1) \\ \mathrm{Im}(\widetilde{J}_2) \\ \vdots \\ \mathrm{Im}(\widetilde{J}_k) \end{Bmatrix} = \begin{Bmatrix} -\gamma\omega \left(M_{1,1}\mathrm{Re}(\widetilde{I}_1) + M_{1,2}\mathrm{Re}(\widetilde{I}_2) + \ldots M_{1,c}\mathrm{Re}(\widetilde{I}_c) \right) \\ -\gamma\omega \left(M_{2,1}\mathrm{Re}(\widetilde{I}_1) + M_{2,2}\mathrm{Re}(\widetilde{I}_2) + \ldots M_{2,c}\mathrm{Re}(\widetilde{I}_c) \right) \\ \vdots \\ -\gamma\omega \left(M_{k,1}\mathrm{Re}(\widetilde{I}_1) + M_{k,2}\mathrm{Re}(\widetilde{I}_2) + \ldots M_{k,c}\mathrm{Re}(\widetilde{I}_c) \right) \\ \gamma\omega \left(M_{1,1}\mathrm{Im}(\widetilde{I}_1) + M_{1,2}\mathrm{Im}(\widetilde{I}_2) + \ldots M_{1,c}\mathrm{Im}(\widetilde{I}_c) \right) \\ \gamma\omega \left(M_{2,1}\mathrm{Im}(\widetilde{I}_1) + M_{2,2}\mathrm{Im}(\widetilde{I}_2) + \ldots M_{2,c}\mathrm{Im}(\widetilde{I}_c) \right) \\ \vdots \\ \gamma\omega \left(M_{k,1}\mathrm{Im}(\widetilde{I}_1) + M_{k,2}\mathrm{Im}(\widetilde{I}_2) + \ldots M_{k,c}\mathrm{Im}(\widetilde{I}_c) \right) \end{Bmatrix} \tag{2.26}$$

where the coefficient matrix is made up of the full and diagonal submatrices, [**F**] and [**D**]

$$[\mathbf{F}] = \begin{bmatrix} \gamma\omega(M_{1,1}S_1) & \gamma\omega(M_{1,2}S_2) & \ldots & \gamma\omega(M_{1,k}S_k) \\ \gamma\omega(M_{2,1}S_1) & \gamma\omega(M_{2,2}S_2) & \ldots & \gamma\omega(M_{2,k}S_k) \\ \vdots & \vdots & \ddots & \vdots \\ \gamma\omega(M_{k,1}S_1) & \gamma\omega(M_{k,2}S_2) & \ldots & \gamma\omega(M_{k,k}S_k) \end{bmatrix} \tag{2.27}$$

$$[\mathbf{D}] = \begin{bmatrix} 2\pi(r_{loop})_1 & 0 & \ldots & 0 \\ 0 & 2\pi(r_{loop})_2 & \ddots & \vdots \\ \vdots & \ddots & \ddots & 0 \\ 0 & \ldots & 0 & 2\pi(r_{loop})_k \end{bmatrix}. \tag{2.28}$$

The linear system is solved using the `solve` function in the `linalg` linear algebra package in NumPy.

3.4.1 Mutual inductance

Setting up the linear system in equation (2.26) requires computing the mutual inductance between the discretized sample rings and the coil rings. Block number eight in Figure 3.1 illustrates the `mutualInduc` function that computes the mutual inductance between two rings given their radii and distance from each other.

The mutual inductance between two rings is computed by integrating equation (2.20). This can be done in various ways and El-Kaddah and Szekely [4] do not specify which method they use in their model implementation. Fromm and Jehn [6] make use of a formula from Smythe [15] for the mutual inductance between two rings in their simplified analytical levitation cell model. This formula is derived for the case where the one ring is small in comparison with the other. Tarapore and Evans [17] use standard ring-ring formulas to compute mutual inductance between conducting

rings. These ring-ring formulas are solutions of equation (2.20) in terms of elliptic integrals for the specific case of coaxial rings. Another option is numerical integration using the trapezoidal rule, but this requires a large number of increments to find an accurate answer and consequently requires significantly more computational time than the other two methods. All three of these methods are implemented. The elliptic integrals are computed using the `ellipk` and `ellipe` functions from the special functions package in SciPy. Figure 3.2 shows the mutual inductance computed by each method for a range of size ratios between the two loops. Table 3.2 gives the typical time it takes to do one mutual inductance computation using each of these three methods.

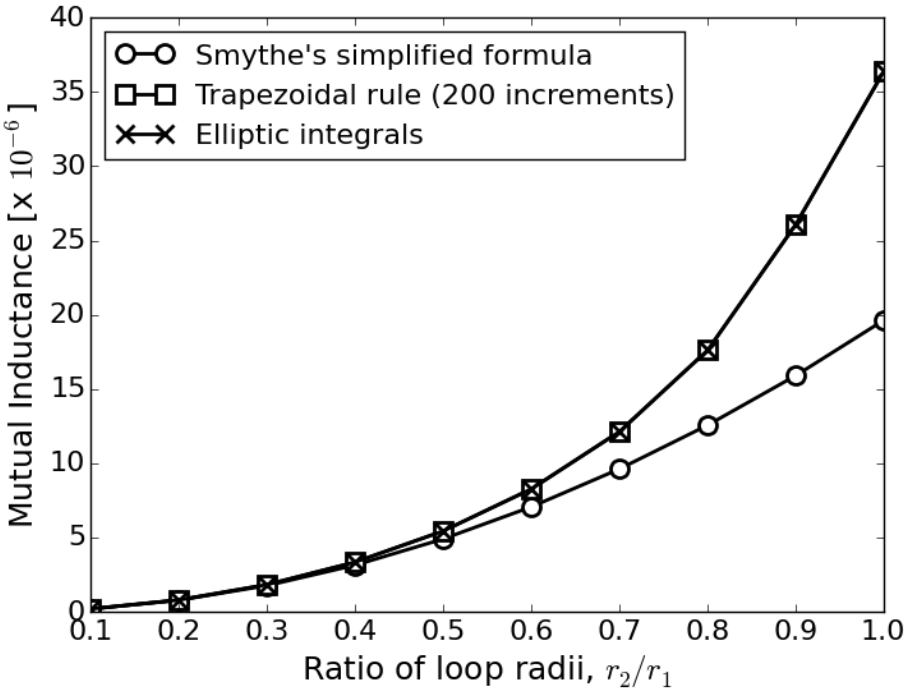

Figure 3.2: Different methods to compute mutual inductance for a range of relative loop sizes.

Table 3.2: Typical computation time required for one mutual inductance calculation using three different methods.

Method	Time [s]
Smythe's simplified formula	0.001
Trapezoidal rule (200 increments)	5.15
Elliptic integrals	0.0001

Figure 3.2 shows that Smythe's simplified formula gives a different result than the elliptic and trapezoidal integration when the ratio between the two loop sizes becomes close to one. This is to be expected, since the formula is derived based on

the assumption that one loop is much larger than the other. In equation (2.26), all the diagonal terms in the **F**-matrix contain self-inductance terms. It is therefore also necessary to compute the self-inductance of the discretized sample loops and self-inductance implies a loop radius ratio of one. The mutual inductance formula utilized by Fromm and Jehn [6] will therefore provide less accurate answers in the current application than the other two methods.

Figure 3.2 further shows that the elliptic and trapezoidal integration gives the same value for the mutual inductance across all size ratios. Table 3.2 however shows that the elliptic integral method is a significantly faster computation than the trapezoidal rule method. The elliptic integral method is therefore chosen to compute the mutual inductances in our levitation cell model. The other two methods are used in unit tests for the mutual inductance function to compare the elliptic integral calculation against and ensure that it is implemented correctly.

The mutual inductance of two coaxial rings in terms of elliptic integrals is given by Ramo et al. [13] as

$$M_{ij} = \mu\sqrt{ab}\left[\left(\frac{2}{k} - k\right)K(k) - \frac{2}{k}E(k)\right] \tag{3.1}$$

where $E(k)$ and $K(k)$ are the complete elliptic integrals of the first and second kinds respectively. μ is the magnetic permeability of the material between two coaxial rings with radii a and b, separated by distance d. k is calculated from

$$k = \sqrt{\frac{4ab}{d^2 + (a+b)^2}}. \tag{3.2}$$

The self-inductance of a ring is given by Ramo et al. [13] as

$$M_{ij} = \mu(2a - c)\left[\left(1 - \frac{k^2}{2}\right)K(k) - E(k)\right] \tag{3.3}$$

where a is the loop radius and c is the radius of the conductor itself. Since the discretized sample loops do not have circular cross-sections, an effective conductor radius is calculated using the non-circular cross-sectional area of the conductor in the formula for the area of a circle and solving for the radius. For the self-inductance case, k is computed from

$$k = \sqrt{\frac{4a(a-c)}{(2a-c)^2}}. \tag{3.4}$$

3.5 Magnetic flux computation

The magnetic flux density field is computed by the `solveMagField` function in block number 10 of Figure 3.1. Some preliminary work has to be done before the magnetic flux density can be computed and this is done in the `discSample`, `coilRprime` and `convert2cart` functions given in blocks 3, 6 and 9 respectively.

The magnetic flux field is computed from

$$\mathbf{B} = \frac{\mu_0}{4\pi} \int_V \frac{\mathbf{J} \times \hat{\boldsymbol{r}}}{|\boldsymbol{r}|^2} dV. \tag{2.29}$$

Numerically solving equation (2.29) is a different approach to obtaining the magnetic flux density than that taken by El-Kaddah and Szekely [4]. El-Kaddah and Szekely propose first integrating the current density field to find the vector potential field and then differentiating to find the flux density field. Instead, we immediately integrate the current density field according to equation (2.29). This reduces the computation to only one integration step, instead of an integration step as well as a differentiation step. Removing the differentiation step is advantageous because numerical differentiation has limited accuracy due to increased round-off error with fine meshes [2] as explained in Section 2.2.3.

Three aspects of equation (2.29) have to be addressed for it to be solved numerically in the model: the current density $\mathbf{J}$ which is solved for only one non-zero component in the ϕ-direction has to be converted to the Cartesian coordinate system, the separation vectors $\boldsymbol{r}$ for each point in the solution domain have to be computed, and the cross product computation has to be vectorized to speed up the computation. The `convert2cart` function (block 9, Figure 3.1) calculates x- and y-components of the current density in the ϕ-direction as

$$\begin{aligned} J_x &= -J_\phi \sin(\phi) \\ J_y &= J_\phi \cos(\phi). \end{aligned} \tag{3.5}$$

The other two aspects of computing the separation vectors and vectorizing the cross product are now explained in more detail.

3.5.1 Separation vectors

Equation (2.29) contains the unit separation vector $\hat{\boldsymbol{r}}$ and the magnitude of the separation vector, $|\boldsymbol{r}|$ [1]. In the case of the levitation cell model the field points are all the points where we want to compute the magnetic flux density, i.e. all the cell centers on one rotationally symmetric plane of the sample. Figure 3.3a shows all the field points for a sample with a $4 \times 4 \times 8$ discretization in the r-, θ-, and ϕ-directions.

[1] Separation vectors are explained in section 2.2.3.

The source points to be considered for the calculation of each field point are all the points carrying electric charge in the vicinity of the field point. For the levitation cell model, this will be all the finite volume elements carrying current, including both the current in the coil and the induced current in the sample. Figure 3.3b shows all the source points for a sample with a $4 \times 4 \times 8$ discretization in the r-, θ-, and ϕ-directions. Figure 3.3c shows all the source points when viewed from the top. Further indicated on this Figure are the single axisymmetric plane of points that are also act as field points.

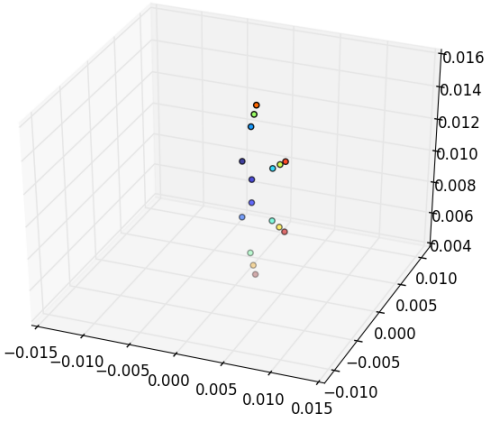

(a) Field points.

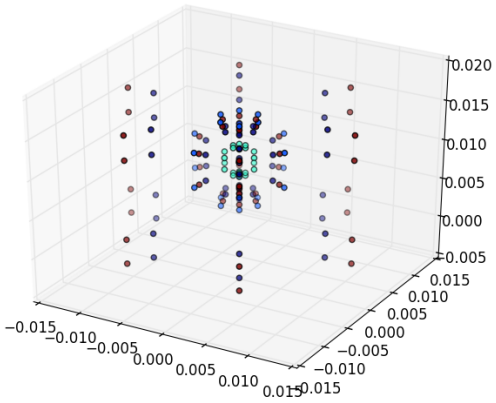

(b) Source points.

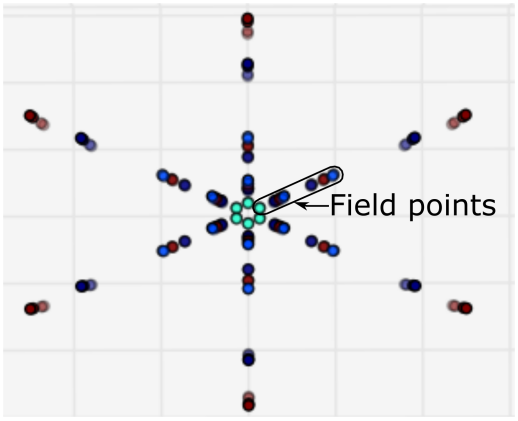

(c) Top view of source points, further indicating which of the source points are also used as field points.

Figure 3.3: Field and source points for a sample with a $4 \times 4 \times 8$ discretization in the r-, θ-, and ϕ-directions.

For each field point where magnetic flux density is to be evaluated, equation (2.29) requires that separation vectors from that field point to all the source points have to be computed. Section 3.8 describes the search for the stable levitation position which requires evaluating the levitation force and consequently the magnetic flux density in the sample at various positions inside the coil. Since all the field points lie

in the sample, the separation vectors between the field points and the source points inside the sample are independent of the sample's position inside the coil. These separation vectors are therefore only computed once by the `discSample` function (block 3, Figure 3.1) and are then saved in an array. Now only the separation vectors between field points and the source points in the coil loops have to be recalculated for each different sample position that is evaluated. This is done by the `coilRprime` function in block number six of Figure 3.1.

3.5.2 Cross product vectorization

The number of cross product computations required for the calculation of the magnetic flux density $\mathbf{B}$ from equation (2.29) quickly increases when the mesh is refined, because to evaluate $\mathbf{B}$ at just one field point requires as many cross products as there are source points in the mesh, and this has to be repeated for every field point. A $4 \times 4 \times 8$ mesh requires 127 cross products for each of the 16 field points. This gives 2038 cross product calculations in total. For a $8 \times 8 \times 16$ mesh with double the number of cells in each direction the total number of cross product calculations required becomes 65472. For finer meshes this computation can therefore take a significant amount of time.

The `cross` function in Python's NumPy package is used for the cross product computation in equation (2.29). This function allows for vectorization if all the vectors that have to be crossed are arranged in matrices. The calculation was first done in a double for-loop where the outer for-loop iterates through all the field points and the inner for-loop through all the source points. The inner for-loop was then removed and replaced with a vectorized cross product computation. A $25 \times 25 \times 25$ case was simulated using both approaches. The time it takes to do the 9765000 cross product calculations in each case is given in Table 3.3.

Table 3.3: Time required for 9765000 vectorized and non-vectorized cross product computations.

	Time [s]
Non-vectorized	1801.1
Vectorized	16.1

The non-vectorized computation takes approximately half an hour, while the vectorized computation takes 16 seconds. This makes a significant difference in the time taken to run the model, especially when taking into consideration that the magnetic flux has to be evaluated for a range of sample positions to find the stable levitation position (see Section 3.8). Vectorization of the cross product computation is therefore considered necessary for developing a useful levitation cell model using the current approach.

3.6 Levitation force computation

After the induced current density and magnetic flux density are computed as described in Sections 3.4 and 3.5, the levitation force acting on the sample is computed by the `samplePos` function (block number five of Figure 3.1) using

$$\mathbf{F} = \mathrm{Re}(\mathbf{J} \times \mathbf{B}). \tag{2.30}$$

This cross product calculation is again vectorized and computed using the `cross` method in the NumPy package. Once the levitation force is known, it is compared to the weight of the sample to determine whether the sample can be levitated and, if stable levitation is possible, what the position of the sample will be inside the coil.

3.7 Absorbed power computation

The power absorbed by the sample is computed using

$$P = \mathrm{Re}\left(\mathbf{J} \cdot \mathbf{J}\right)/\gamma \ . \tag{2.31}$$

We need the induced current density from the computation described in Section 3.4, but also the stable levitation position for the sample, since the power absorbed by the sample is also a function of the sample's position in the coil [14]. The searching procedure to find the stable sample levitation position is described next.

3.8 Searching for the stable sample levitation position

Figure 3.4a shows a simple levitation cell coil geometry where the electrical current flows in opposite directions in each of the two coil loops. The field points inside the sample are also included on the Figure, which is shown at the stable levitation position of the sample. Figure 3.4b gives the levitation force a sample would experience inside this coil at various heights along the coil symmetry axis as predicted by our model implementation. The weight of the sample is also plotted on the same graph.

Levitation is possible in the positions inside the coil where the levitation force is equal to the weight of the sample. In this case there are four positions where the levitation force and weight curves intersect. These points can be computed by subtracting the weight from the levitation force and finding the roots of the result. However, the levitation position is only stable when the gradient of the force is negative, i.e. $dF/dz < 0$ [14]. At a levitation position with a negative

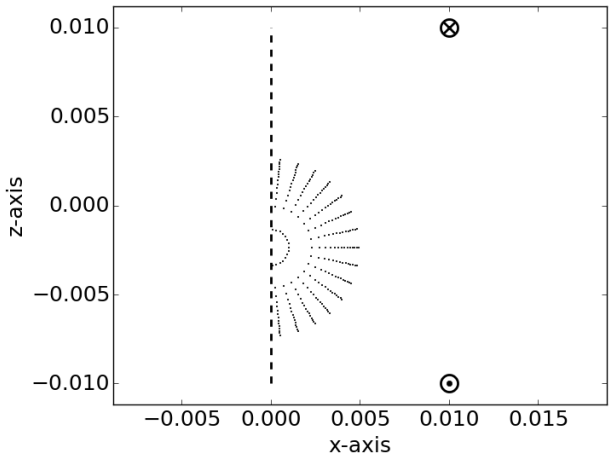

(a) Coil geometry with the field points included in the stable levitation position.

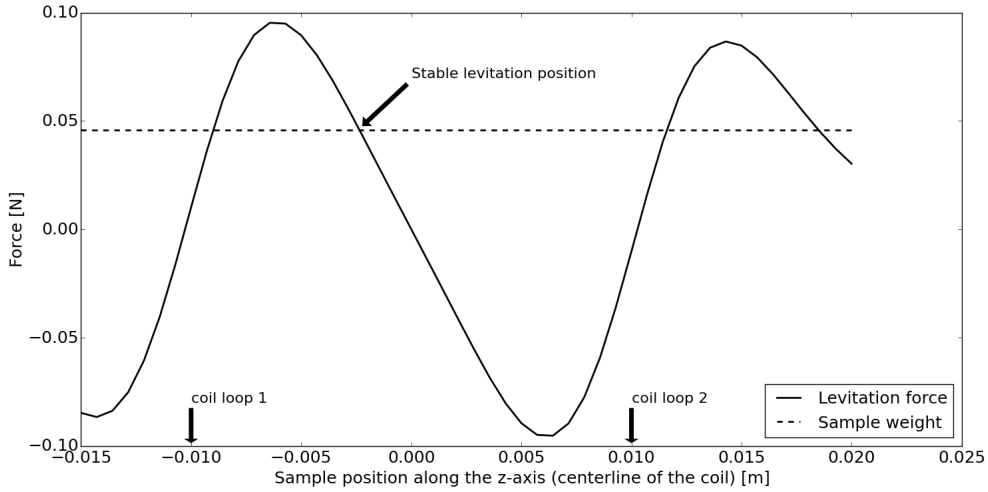

(b) The levitation force experienced by the sample at different heights inside the coil in Figure 3.4a plotted with the sample weight.

Figure 3.4: Finding the sample levitation position.

gradient, moving the sample slightly higher would result in it experiencing a smaller levitation force and it will fall back into its levitation position. Similarly, the sample will experience a larger levitation force slightly below its levitation position which will push it back up. The system is therefore self-correcting when the gradient of the force curve is negative. In Figure 3.4b there are two stable levitation positions, but only one lies inside the coil and this is the levitation position at which the levitation cell should be operating.

The power absorbed by the sample and consequently the sample temperature is a function of the sample's position inside the coil [14]. Therefore the model should be able to find the correct levitation position and then compute the absorbed power and sample temperature in this position. Simply using a numerical technique to find a root of the difference between the levitation force and the sample weight is not adequate because the root that is found depends strongly on the initial guess provided to the algorithm and it is difficult to determine whether the first root that is found is the correct root.

Ensuring that the model finds the correct root therefore requires a combined root-finding and search strategy. The stable root inside the coil should be the root with a negative gradient closest to the bottom of the coil. To search for this root we start on the level of the bottom coil loop and evaluate the force balance in increments of the radius of a single coil loop. Each coil loop contributes to the levitation force and it is therefore assumed that the levitation force will not change sign twice within the height of one coil loop radius. The increment containing the bottom stable root is found when the sign of the force balance changes from positive to negative. A single root is now isolated within the increment size and a bounded root-finding method can now be used to find the exact position of the root. This is achieved by minimizing the square of the force balance

$$\min F_{total} = \min(F_{levitation} - F_{weight})^2 \tag{3.6}$$

using the `SLSQP` algorithm in the `optimize.minimize` package in SciPy. SLSQP is a bounded optimization algorithm which allows the bounds of the increment to be used as the bounds for root-finding. This ensures the correct root that was previously isolated is found.

It is also possible that a specific coil design does not provide a large enough levitation force for the sample to be levitated. In this case the program will search through the entire coil height without finding a change in the sign of the force balance. If this is the case the function in equation (3.6) is still minimized and it will consequently return the position in the coil with the largest levitation force. A message is also printed to the screen indicating that levitation is not possible with the specified coil design and sample combination.

3.9 Temperature calculation and model output

With the absorbed power in the sample levitation position computed, the sample temperature is calculated as described in Section 2.3.3. The heat transfer calculation is done by the `sampleTemp` function (block number 11 in Figure 3.1). The plotting function in block number 12 in Figure 3.1 plots the fields computed in the electromagnetic part of the model using the `PolyCollection` function in matplotlib library for Python. A lumped parameter approach is followed to compute the sample temperature, and therefore only a single average value for the sample temperature is obtained as the output of the heat transfer calculation.

Chapter 4

Model Verification & Validation

This chapter describes the verification of the numerical model implementation described in Chapter 3. This is followed by a validation step where model results are compared with experimental data from literature in order to determine to what extent the model is able to make realistic predictions about levitation cell experiments.

4.1 Model verification

Model results from most of the models described in the literature review in Section 2.2.1 are compared to experimental results or other model results in order to validate the models. However, these reviewed model implementations do not describe verification tests to check whether the model was implemented correctly and as intended. Here we describe a quantitative verification case for a single loop levitation cell coil and how symmetry can be used to qualitatively verify more complex coil designs.

4.1.1 Quantitative verification for a single loop coil

Lorentz force between two parallel wires

The Lorentz force per unit length $F/\Delta L$ experienced by an infinitely long, straight current carrying wire due to the presence of another current carrying wire parallel to it, can be obtained from the analytical expression [7, §5.2.2]

$$\frac{F}{\Delta L} = \frac{\mu_0 I_1 I_2}{2\pi d} \tag{4.1}$$

where I_1 and I_2 are the currents in the two respective wires, μ_0 is the magnetic permeability of free space, and d is the distance between the two parallel wires as illustrated in Figure 4.1a. Figure 4.1b shows the simplest possible levitation cell

design consisting of only a single coil loop and the sample to be levitated. The way in which the sample would be discretized in the model is also indicated on the Figure. In order to use the analytical expression for the Lorentz force between two wires as a verification test for the levitation cell, the levitation cell geometry in Figure 4.1b has to be adapted to be similar to that of the parallel wires in Figure 4.1a.

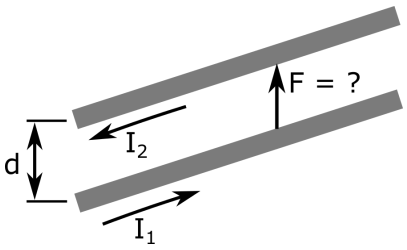

(a) Lorentz force between two parallel wires.

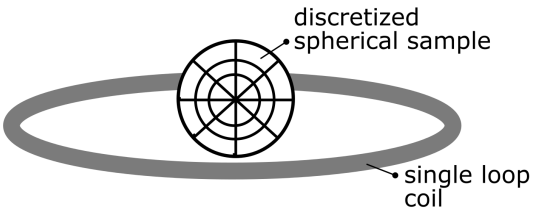

(b) Single loop levitation cell model geometry.

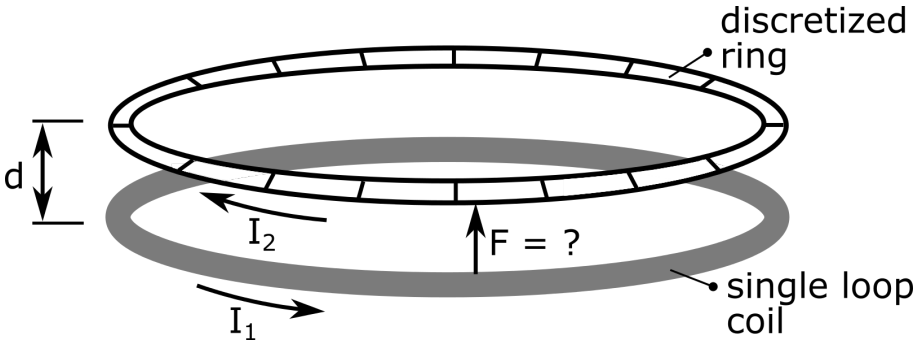

(c) Model geometry for Lorentz force verification.

Figure 4.1: Using the analytical expression for the Lorentz force between two parallel wires to verify the Lorentz force calculation in the levitation cell model.

Figure 4.1c shows how two parallel current conducting loops can be modelled by changing the sample geometry from a discretized sphere to a discretized ring. It can now be expected that as the radii of the two parallel loops are increased, the Lorentz force between the parallel loops should converge towards the Lorentz force between the parallel wires. This can then be used to verify whether the force computation in the levitation cell model is implemented correctly.

In the parallel loop verification test the current in the coil loop is specified and the model then computes the induced current in the discretized loop as well as the Lorentz force between the two loops. The Lorentz force is also computed analytically using equation (4.1) with the values of the specified current in the coil loop, the induced current value obtained from the model and the coil geometry. The value obtained from this analytical calculation is compared to that obtained from the model. This means that this test does not verify the induced current computation. However, the induced current computation is the solution of a set of linear equations and for the case of two parallel loops this linear system reduces to a 2×2 system.

The induced current computation is therefore easily verified by solving the two simultaneous equations in a hand calculation.

The parallel wires test is used to verify the model implementation described in Chapter 3. Two copper loops with cross-sectional radii of 226 mm are modelled with a distance of 0.6 m separating them. The loop radii are increased from 0.5 m to 20 m. An electrical current of 1 A alternating at 27 kHz is specified to flow in the coil loop. The current induced in the discretized loop is computed by the model as a function of the radii of the two loops. The value of the electrical conductivity of the copper loops is assumed to be $\gamma = 5.96 \times 10^7$ S/m.

Since one of the two loops is discretized, a mesh independence study is necessary to ensure that the verification test result will not change when the number of cells in the discretized ring is increased. The largest loop radii would require the most cells and therefore the case with loop radii of 20 m is used for the mesh independence study. The result of the mesh independence study can be seen in Figure 4.2. Based on this result 250 cells are used to model the discretized ring.

Figure 4.3 shows the results of the verification test for the current model implementation. The analytical computation and the model prediction converge to the same force value as the loop radii are increased and it is concluded that the force calculation of the current model implementation is successfully verified for the simplified case of a single loop coil.

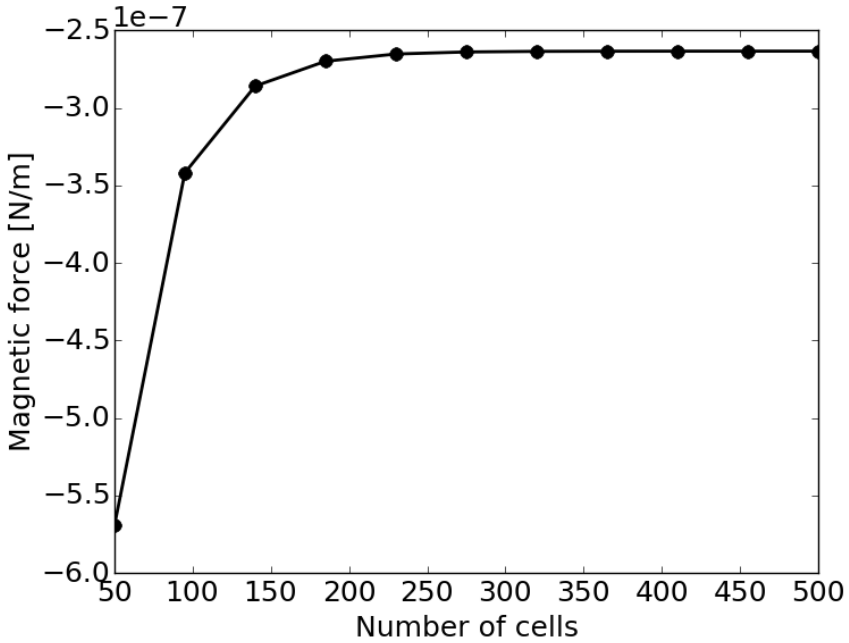

Figure 4.2: Mesh independence study for the parallel wires verification test.

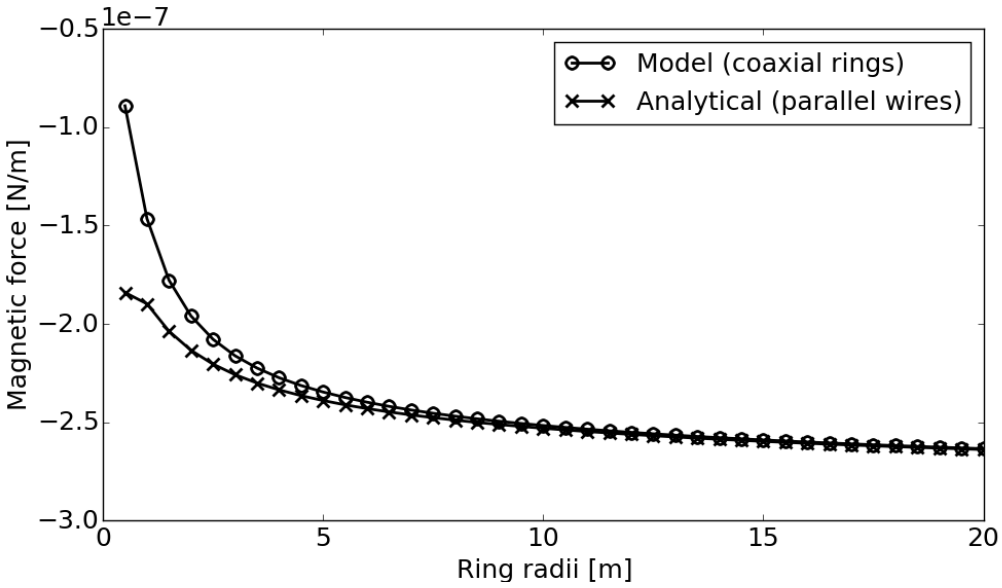

Figure 4.3: Parallel wires verification test result.

Induced current verification

In Section 4.1.1 the levitation force calculation in the model was verified for a simplified case based on the assumption that the model computes the induced current correctly. A hand calculation is now used to verify that the induced current is indeed computed correctly in the model. The induced current is found by solving for $\widetilde{J}_i$ in equation (2.25).

$$\begin{aligned} \mathrm{Re}(\widetilde{J}_i)\,(2\pi r_{loop}) + \omega\gamma \left(\sum_{n=1}^{sample\ loops} Im(\widetilde{J}_n) S_n M_{in} \right) &= -\omega\gamma \left(\sum_{n=1}^{coil\ loops} Re(\widetilde{I}_n) M_{in} \right) \\ \mathrm{Im}(\widetilde{J}_i)\,(2\pi r_{loop}) - \omega\gamma \left(\sum_{n=1}^{sample\ loops} Re(\widetilde{J}_n) S_n M_{in} \right) &= \omega\gamma \left(\sum_{n=1}^{coil\ loops} Im(\widetilde{I}_n) M_{in} \right) \end{aligned} \quad (2.25)$$

The discretized ring has only one cell on the rz-plane, and therefore $i = 1$ and equation (2.25) becomes two simultaneous equations that easily be solved by hand for verification purposes. The parallel loops verification test only consists of one coil loop and one sample loop. Therefore the summation terms in equation (2.25) all consist of only one term.

We now verify the induced current computation for the parallel loops test case described in Section 4.1.1, using loop radii of 10 m. The mutual inductance between the sample ring and the coil loop is found to be $M_{ring,loop} = 3.638 \times 10^{-5}$ using equation (3.1) with $k = 0.99955$, $K(0.999955) = 4.8938$ and $E(0.999955) = 1.00197$. The self-inductance of the sample ring is found as $M_{ring,ring} = 4.750 \times 10^{-5}$ using

equation (3.3) with $k = 0.99993$, $K(0.99993) = 5.8234$ and $E(0.99993) = 1.00037$. Substituting this together with the values used for the parallel loops test as given in Section 4.1.1 into equation (2.25), results in a phasor value for the induced current of $\widetilde{J}_{ring} = -4.77 - 3.87 \times 10^{-6}i$ A/m^2. This is approximately equal to the induced current value of $\widetilde{J}_{ring} = -4.73 - -3.82 \times 10^{-6}i$ A/m^2 predicted by the model. The induced current calculation is therefore successfully verified for the case of a single loop coil.

The power absorbed by the sample is computed from the current induced in the sample. This is then used to find the sample temperature from a simple energy balance. Verifying the induced current calculation therefore also verifies the most complicated part of the temperature calculation.

4.1.2 Qualitative verification for a multi-loop coil

Verifying the model implementation for more complex coil designs is challenging, but symmetry can be used to qualitatively verify the model for multi-loop coil designs. The coil geometry in Figure 4.4 used by El-Kaddah and Szekely [4] is an example of a symmetrical levitation cell coil design.

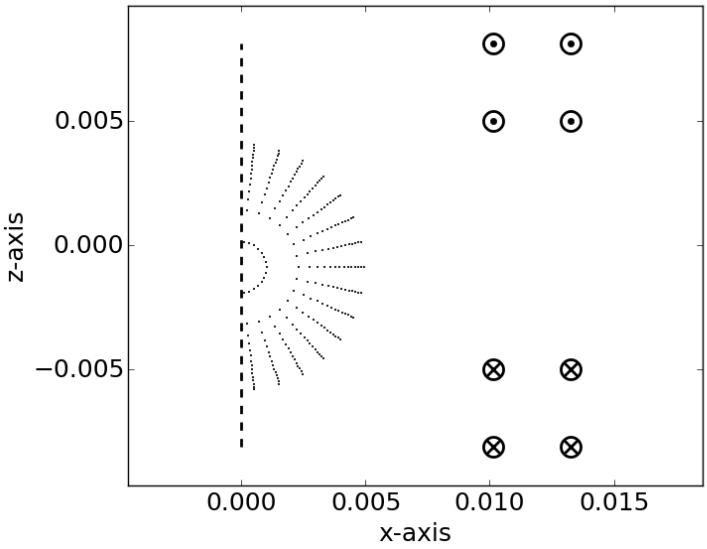

Figure 4.4: Symmetrical coil geometry used by El-Kaddah and Szekely [4].

The coil geometry in Figure 4.4 is symmetrical about $z = 0$, but with the electrical current in the top loops flowing in the opposite direction to the current in the bottom loops. It can therefore be expected that the levitation force magnitude along the centerline of the coil should be symmetric about $z = 0$ but with the force acting in opposite directions due to the opposite current directions. This is used as a qualitative verification test for a symmetrical, multi-loop coil design.

A converged mesh is required in order to model the symmetrical coil design in Figure 4.4. Figure 4.5 shows the results from a mesh independence study on the predicted sample levitation position for the coil geometry in Figure 4.4. The variation in sample levitation position is less than a millimetre between all the plotted mesh densities, and a mesh with $15 \times 15 \times 15 = 3375$ cells is chosen for the model. The coil design and material properties used to model the symmetrical levitation cell of El-Kaddah and Szekely [4] are given in Table 4.1.

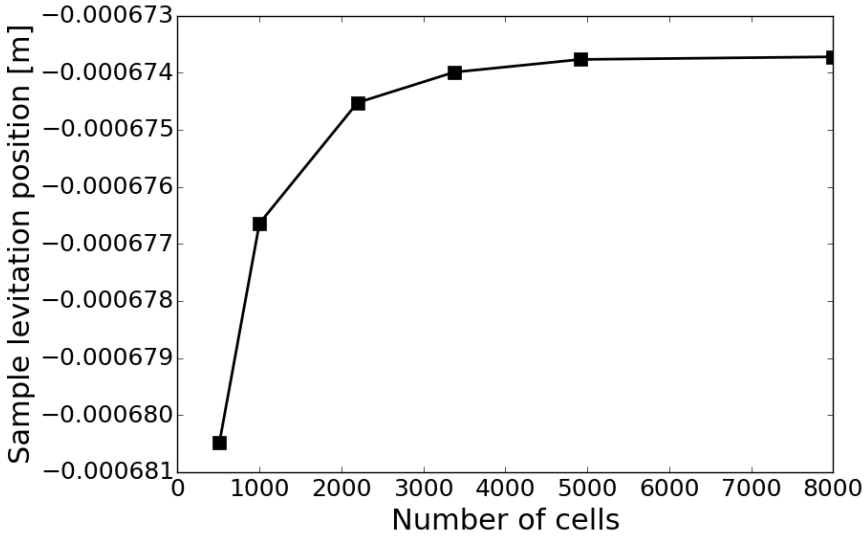

Figure 4.5: Model prediction for the sample levitation positions as the number of cells are increased.

Table 4.1: Coil parameters and material properties used to model the El-Kaddah and Szekely coil design.

Coil geometry

Loop nr	Radius r [m]	Height h [m]	Current direction, k
1	0.01015	- 0.0081	1.0
2	0.01325	- 0.0081	1.0
3	0.01015	- 0.005	1.0
4	0.01325	- 0.005	1.0
5	0.01015	0.005	- 1.0
6	0.01325	0.005	- 1.0
7	0.01015	0.0081	- 1.0
8	0.01325	0.0081	- 1.0

Coil properties

Property	Value	Source
Coil current	400 A	
Frequency	450 kHz	[4]
Tube radius	0.00155 m	

Iron sample properties

Property	Value	Source
Emissivity, ε	0.7	[3]
Electrical conductivity, γ	1×10^7 S/m	
Magnetic permeability, μ	$4\pi \times 10^{-7}$ H/m	
Sample radius, R	3.1 mm	[4]
Density, ρ	7870.0 kg/m^3	[3]
Liquidus temperature, T_m	1810.0 K	[3]

Argon atmosphere properties

Property	Value	Source
Fluid temperature, T_f	298 K	[14]
Surroundings temperature, T_s	298 K	[14]
Thermal conductivity, k	152×10^{-3} W/(mK)	[14]
Velocity, v	0.0184 m/s	[14]
Density, ρ_f	0.1625 kg/m^3	[14]
kinematic viscosity, ν	199×10^{-7} m^2/s	[14]
Specific heat, C_p	520.3 J/kgK	[3]

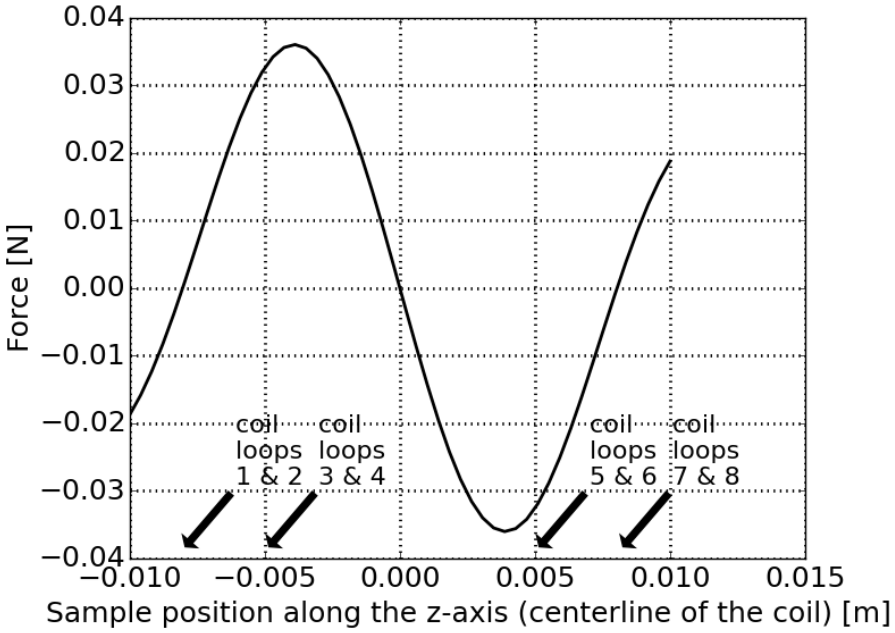

Figure 4.6: Predicted levitation force along the central axis of the symmetrical coil geometry used by El-Kaddah and Szekely [4]. The coil is symmetric around $z = 0$.

Figure 4.6 shows the model prediction for the levitation force along the central axis of the coil, using 3375 cells. The coil geometry is symmetric around $z = 0$ and Figure 4.6 shows that this is also the case for the magnitude of the predicted levitation force. The levitation force is acting in opposite directions on either side of the symmetry plane due to the opposite directions of the current in the coil loops. The levitation force calculation in our model is therefore successfully qualitatively verified for a multi-loop symmetrical coil geometry.

4.2 Model validation

4.2.1 Sensitivities in levitation cell modelling

There are two sources of uncertainty in levitation cell experiments that make the validation of model predictions against experimental results challenging. The material properties at the high temperatures where the levitation cell operates are unknown. The ultimate purpose of the levitation cell is to find a way to obtain these high temperature material properties, because they are not readily available in literature and are difficult or impossible to measure without a contactless environment like the one provided by a levitation cell. Modelling a levitation cell experiment does however require knowledge about the properties of the materials in the model at the operational temperature. These values are therefore estimated, but this results in the first source of uncertainty in the model validation.

The second source of uncertainty is the magnitude of the current supplied to the levitation cell coil. The power supplied to the levitation cell is usually known from the power supply setting at which it operates, but the electrical current in the coil is not necessarily known. Further, the large magnitude and high frequency of the coil current makes it difficult to measure experimentally and levitation cells are often not instrumented for this measurement [4, 10]. The electrical current in the coil is however an input variable in the model. El-Kaddah and Szekely [4] back calculate the coil current during experiments from their model prediction of the sample levitation position and temperature. However, this method of using model results to determine the experimental conditions means that the model is never independently validated against experimental results. It would be preferable to first independently validate the model against experimental results and then use the validated model to determine the experimental conditions of other experiments. One possible approach to determine the current in the coil during experiments is that of Moghimi et al. [10] who use a measured value of the electrical resistance of the coil together with the power setting to compute the coil current.

The interesting question therefore becomes whether the model can still be used to make useful predictions and develop practical levitation cell designs despite these uncertainties. Are there certain characteristics of the levitation cell that are independent of these uncertain parameters, which can be used to design levitation cell experiments for? We therefore use our verified model implementation to investigate the influence that changes in these uncertain parameters have on the levitation force curve predicted by the model.

The temperature dependent material properties involved in the levitation force calculation are the magnetic permeability, the electrical conductivity of the sample and the density of the sample. Figure 4.7 shows the effect of a 10% and 50% increase and decrease of the values of these three temperature dependent material properties as well as the coil current on the force along the central axis of the coil of given in Figure 4.4. The sample density is not directly involved in the levitation force calculation, but changes in sample density will result in changes in the sample radius - which is used in the calculation. The effect of changes in the sample density is therefore investigated by varying the sample radius.

It can be seen from Figure 4.7 that changes in these uncertain parameters affect the amplitude of the force curve, but not the position of the minimum and maximum values where the gradient of the force curve changes. This is significant because a negative force curve gradient at the levitation position is a requirement for stable levitation. It can be concluded from Figure 4.7 that the size of the stable levitation region is independent of the uncertain material property values and coil current magnitude. It is therefore still possible to use the model to design levitation cells for stable levitation, despite uncertainty about the temperature dependent material property values and coil current magnitude.

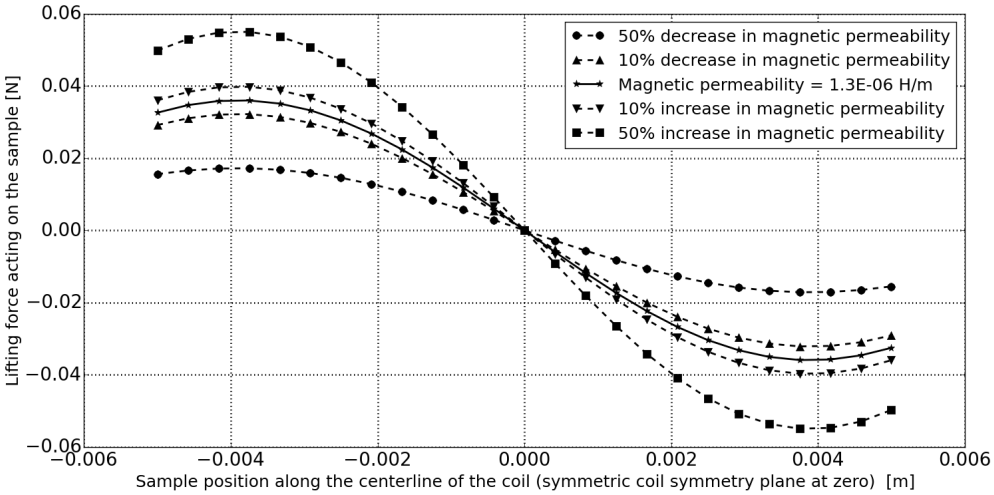

(a) Varying magnetic permeability.

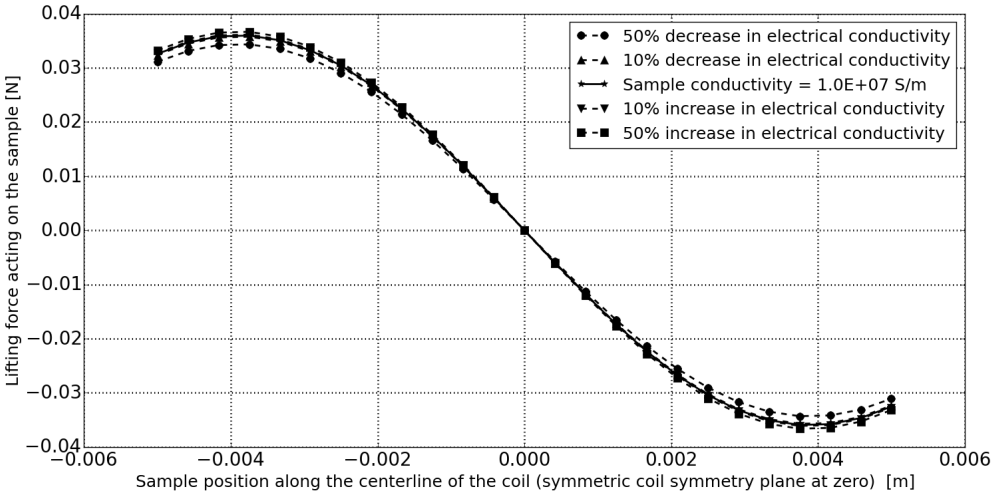

(b) Varying the electrical conductivity of the sample.

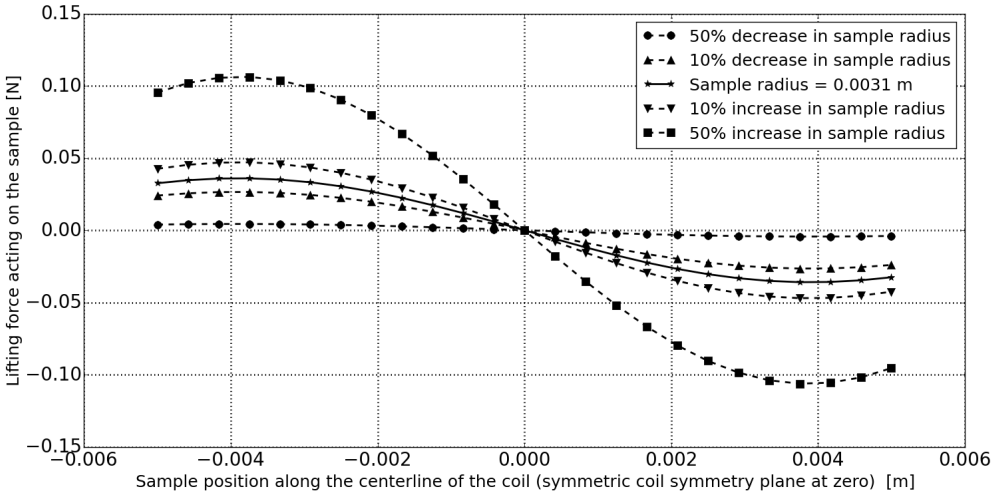

(c) Varying sample radius.

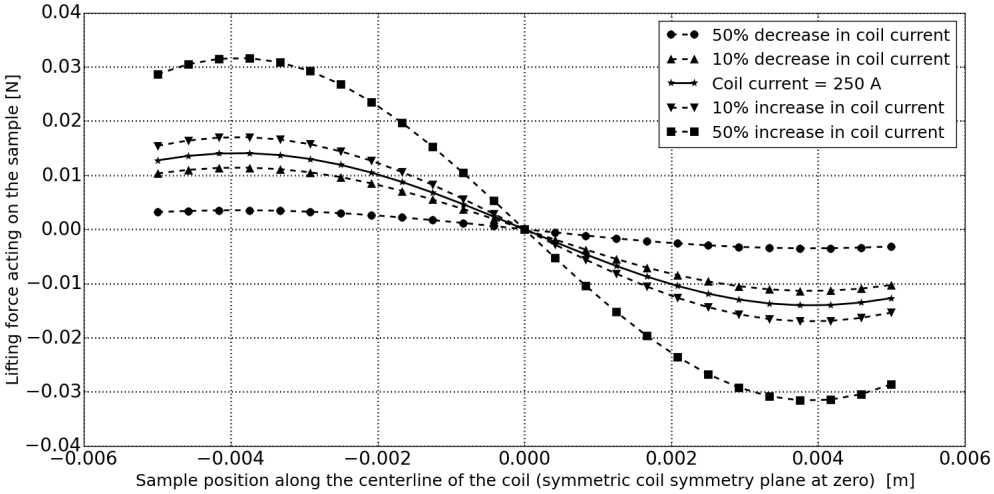

(d) Varying coil current magnitude.

Figure 4.7: Effect of changes in uncertain model parameters on the levitation force along the central axis of the coil.

4.2.2 Levitation force validation against experimental data of Fromm and Jehn [6]

Fromm and Jehn [6] provide experimental results for the levitation force along the centerline of a single-loop coil using spherical samples of various diameters. Force predictions from the current model implementation are validated against these experimental results. The coil geometry and current as well as the properties of the sample and surrounding atmosphere used to model the Fromm and Jehn [6] experiments are given in Table 4.2. Figure 4.8 gives the results of the mesh independence study for this model. The sample is discretized into $20 \times 20 \times 20 = 8000$ cells to obtain the model results used for validation.

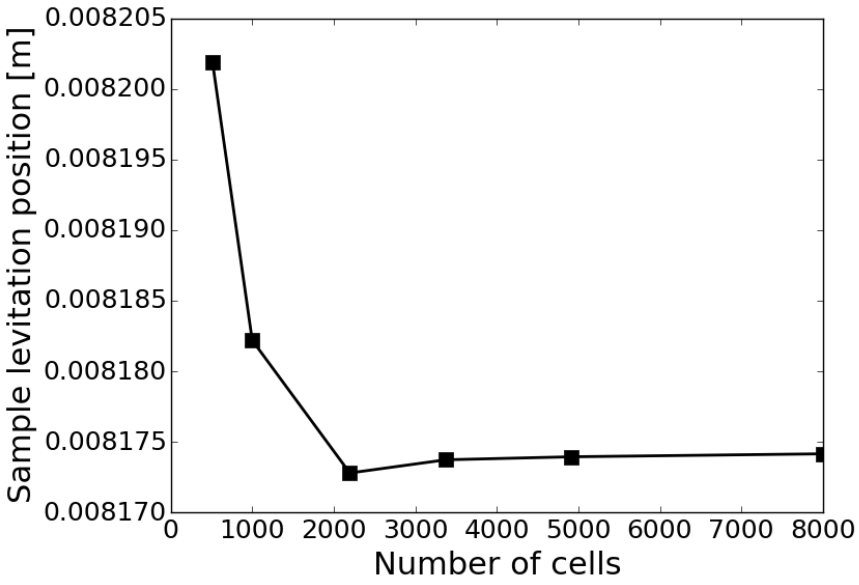

Figure 4.8: Predicted levitation position with increasing mesh density for the single loop coil used in the experiments by Fromm and Jehn [6].

Comparisons of the levitation force predictions of current model implementation with the experimental results of Fromm and Jehn [6] are given in Figure 4.9. Of the possible uncertain model parameters discussed in Section 4.2.1, the magnetic permeability and the electrical conductivity of the sample are not specified by Fromm and Jehn [6]. Based on Figure 4.7b, variations in the electrical conductivity of the sample are not expected to have a large influence on the levitation force predicted by the model.

The magnetic permeability of air is first used to model the Fromm and Jehn [6] experiments (Figure 4.9a). The value of the magnetic permeability is then adjusted up and down and Figure 4.9b shows that using the model with a value of 1.18 times the magnetic permeability of air shows good agreement with the levitation force measurements of Fromm and Jehn [6]. The magnetic permeability value used in the levitation cell model represents a combination of the magnetic permeability of the sample and that of the atmosphere around it. The magnetic permeability of copper is similar to that of air. Although the calibrated value is 18 % higher than the magnetic permeability of air and copper, magnetic permeability is expected to vary with changes in temperature and therefore an 18% variation for copper at high temperatures is still considered feasible. The levitation force prediction of the current model implementation is therefore successfully validated against experimental results, provided that allowance is made for calibration of the uncertain high temperature material properties contained in the model.

Table 4.2: Coil parameters and material properties used with the current model implementation to model the single-loop coil experiments of Fromm and Jehn [6].

Coil geometry

Loop nr	Radius r [m]	Height h [m]	Current direction, k
1	0.021	0.0	1.0

Coil properties

Property	Value	Source
Coil current	500 A	[6]
Frequency	270 kHz	[6]
Tube radius	0.003 m	

Copper sample properties

Property	Value	Source
Emissivity, ε	0.11	[3]
Electrical conductivity, γ	5.96×10^7 S/m	
Magnetic permeability, μ	$4\pi \times 10^{-7}$ H/m	
Sample radius, R	5, 6, 7.5, 10 mm	[6]
Density, ρ	8933.0 kg/m^3	[3]
Liquidus temperature, T_m	1356 K	

Argon atmosphere properties

Property	Value	Source
Fluid temperature, T_f	298 K	[14]
Surroundings temperature, T_s	298 K	[14]
Thermal conductivity, k	152×10^{-3} W/(mK)	[14]
Velocity, v	0.0184 m/s	[14]
Density, ρ_f	0.1625 kg/m^3	[14]
kinematic viscosity, ν	199×10^{-7} m^2/s	[14]
Specific heat, C_p	520.3 J/kgK	[3]

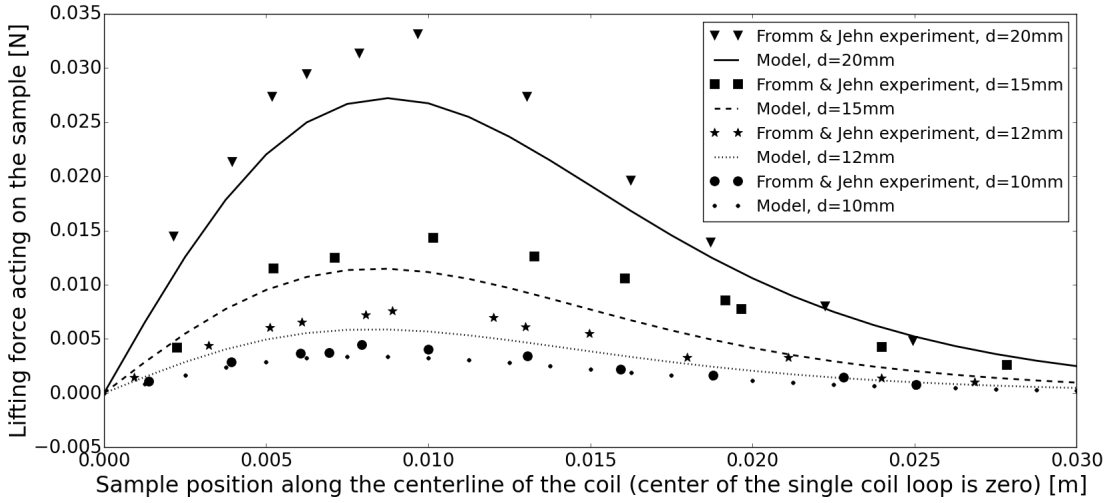

(a) $\mu = \mu_0 = 4\pi \times 10^{-7} = 1.26 \times 10^{-6}$ H/m

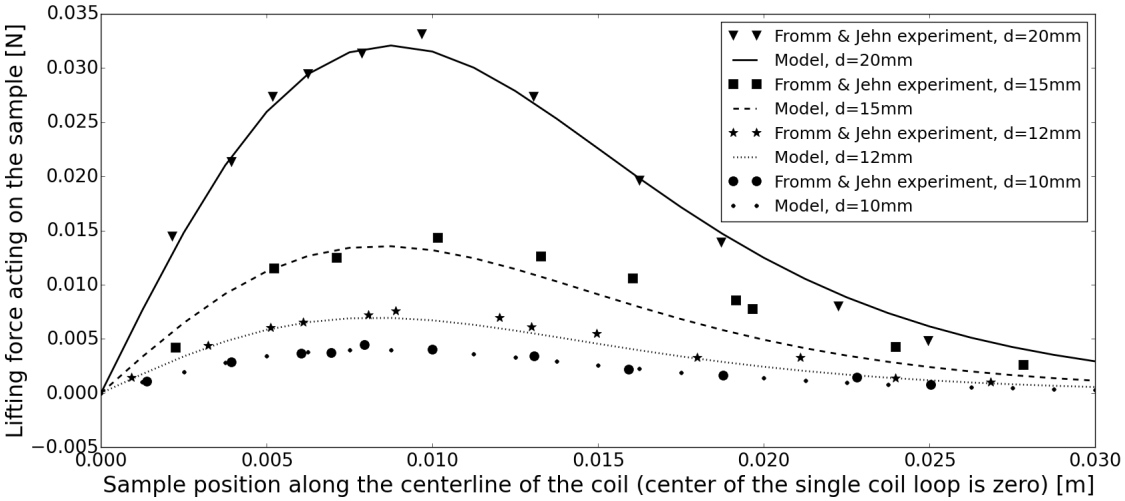

(b) $\mu = 1.18 \times \mu_0 = 1.18 \times (4\pi \times 10^{-7}) = 1.48 \times 10^{-6}$ H/m

Figure 4.9: Model predictions for the levitation force compared to experimental measurements of Fromm and Jehn [6] for spherical samples of various diameters. The magnetic permeability used in the model is that of free space in Figure 4.9a and 1.18 times the magnetic permeability of free space in Figure 4.9b.

4.2.3 Temperature validation against experimental results of Royer et al. [14]

Royer et al. compare their model temperature predictions for a range of coil current magnitudes with experimental results. The experimental results used by Royer et al. [14] are now compared with temperature predictions of the current model implementation. The coil design and material properties used to model the Royer et al. [14] case are given in Table 4.3.

Table 4.3: Coil parameters and material properties used with the current model implementation to model the levitation cell experiment reported by Royer et al, [14].

Coil geometry

Loop nr	Radius r [m]	Height h [m]	Current direction, k
1	0.012	0.0	1.0
2	0.016	0.0	1.0
3	0.012	0.004	1.0
4	0.016	0.004	1.0
5	0.020	0.004	1.0
6	0.012	0.012	0.0
7	0.016	0.012	0.0

Coil properties

Property	Value	Source
Coil current	170 A	[14]
Frequency	178 kHz	[14]
Tube radius	0.0032 m	[14]

Aluminum sample properties

Property	Value	Source
Emissivity, ε	0.1	[14]
Electrical conductivity, γ	4.573×10^6 S/m	[14]
Magnetic permeability, μ	$4\pi \times 10^{-7}$ H/m	[14]
Sample radius, R	5 mm	[14]
Density, ρ	2702.0 kg/m^3	[3]
Liquidus temperature, T_m	933 K	

Argon atmosphere properties

Property	Value	Source
Fluid temperature, T_f	298 K	[14]
Surroundings temperature, T_s	298 K	[14]
Thermal conductivity, k	152×10^{-3} W/(mK)	[14]
Velocity, v	0.0184 m/s	[14]
Density, ρ_f	0.1625 kg/m^3	[14]
kinematic viscosity, ν	199×10^{-7} m^2/s	[14]
Specific heat, C_p	520.3 J/kgK	[3]

The sample is discretized into 30 increments in each of the spherical coordinate directions resulting in a mesh with 27000 cells. The discretization is chosen based on the results of the mesh independence study shown in Figure 4.10. Figure 4.10

shows that an discretization error of five degrees or less is expected in temperature predictions using this mesh density.

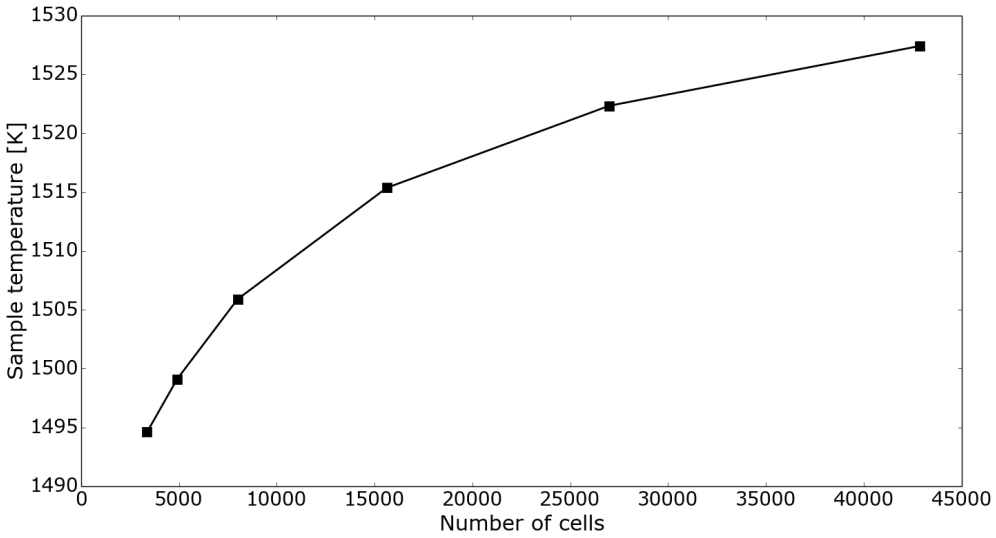

Figure 4.10: Predicted sample temperature with increasing mesh density for the experimental case of Royer et al. [14].

Figure 4.11 shows the comparison between the model predictions for the sample temperature and the sample temperature measured at different coil current magnitudes by Royer et al. [14]. In Figure 4.11a the material properties used with the model are those reported by Royer et al. [14] and given in Table 4.3. However, as is the case with modelling the levitation force, uncertainty exists around the values of a number of material properties used in the temperature model. In computing the absorbed power, the value of the magnetic permeability of the sample is uncertain, and the effect of the temperature dependence of the sample density and electrical conductivity is not taken into account. Large uncertainty exists around the emissivity value used in the radiation heat loss calculation, since only a general emissivity value for the sample material is used and view factors are not considered. It is also difficult to obtain the values of the surrounding fluid properties, especially the thermal conductivity of the fluid, which are used to compute the convection heat loss from the sample. The sample temperature calculation further depends on the stable levitation position of the sample inside the coil, and therefore also on the material properties used in the levitation force calculation. Figure 4.12 shows the effect of changes in some material properties as well as the sample position on the sample temperature prediction. It can be seen that only the sample position influence the gradient of the temperature versus coil current curve.

In the model prediction for the sample temperature as given in Figure 4.11a, the model generally predicts the sample to be hotter than it is observed to be experimentally. Additionally, the sample temperature predicted by the model continues to decrease as the coil current is increased, while the measured sample temperatures reach a minimum temperature at 280 A, after which the sample temperature again

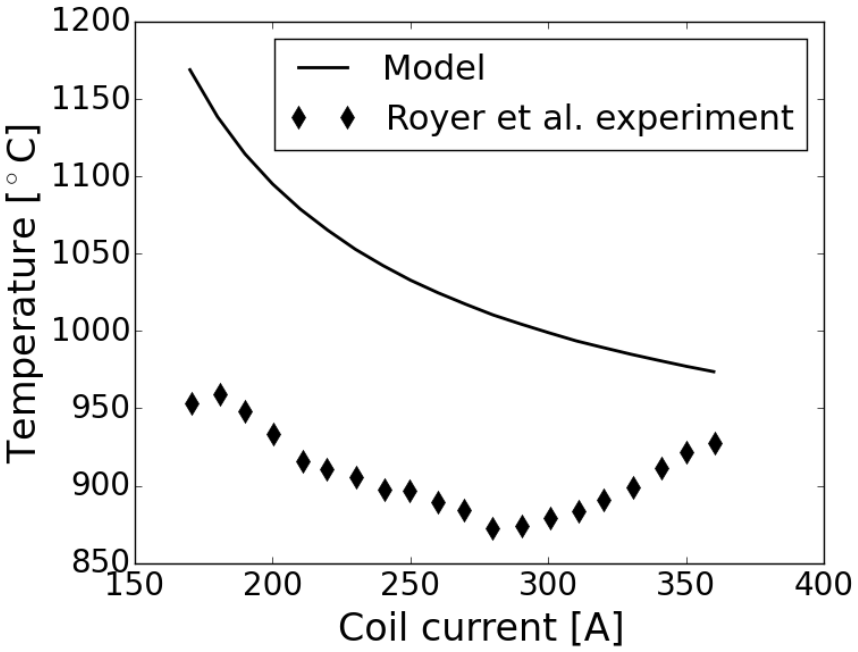

(a) $\varepsilon = 0.1$

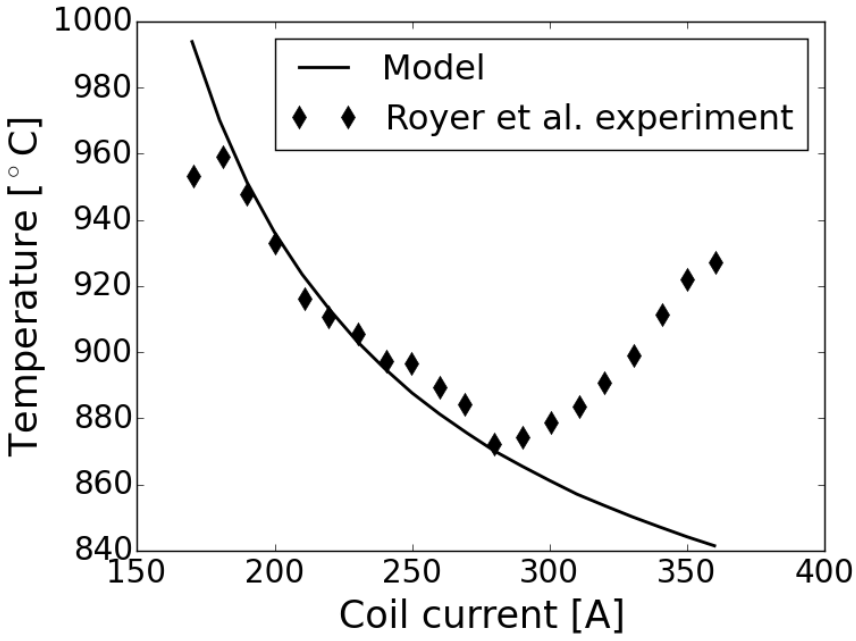

(b) $\varepsilon = 0.21$

Figure 4.11: Current model temperature predictions compared to experimental results of Royer et al. [14]. In Figure 4.11a the emissivity value reported by Royer et al. is used and in Figure 4.11b the emissivity value is increased to reduce the predicted sample temperature.

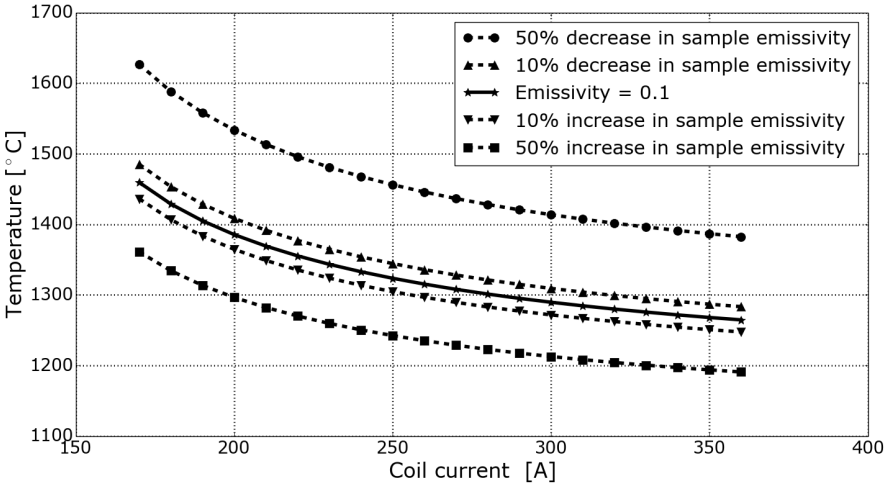

(a) Varying the emissivity of the sample.

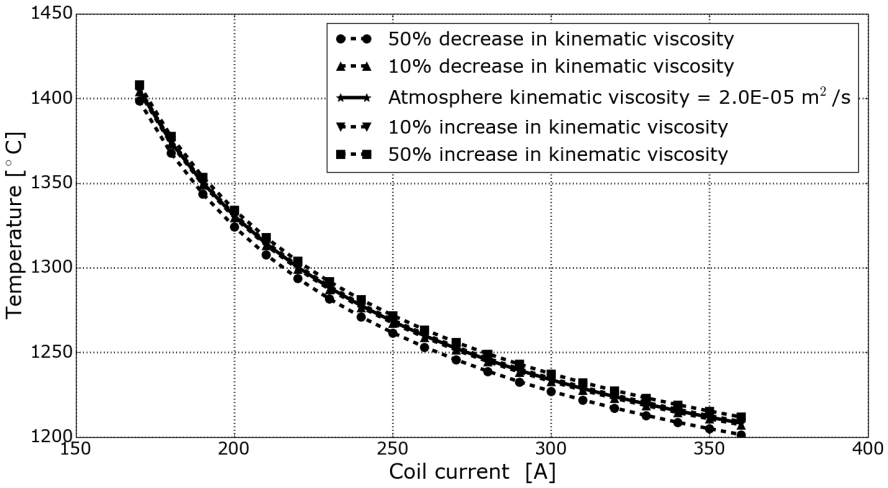

(b) Varying kinematic viscosity of the fluid around the sample.

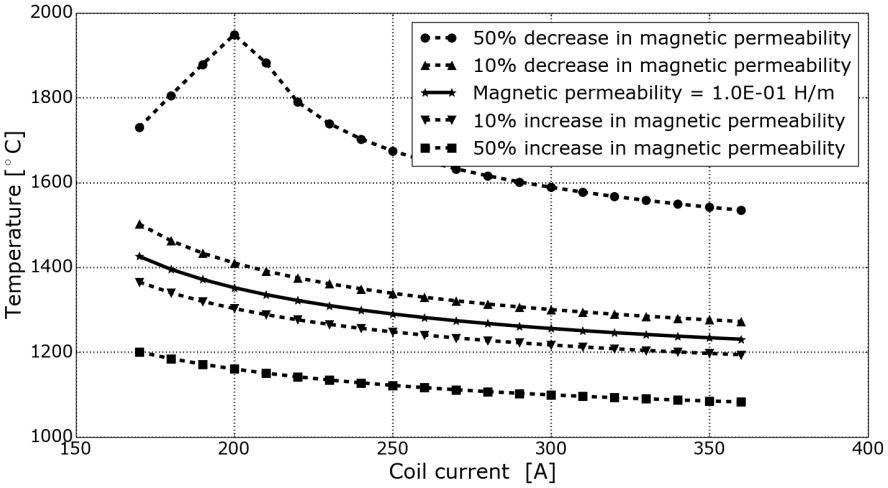

(c) Varying the magnetic permeability.

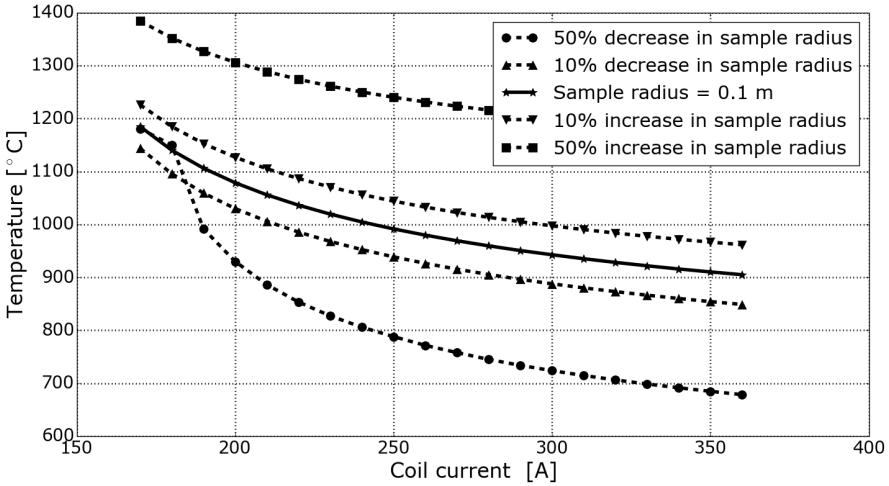

(d) Varying sample radius.

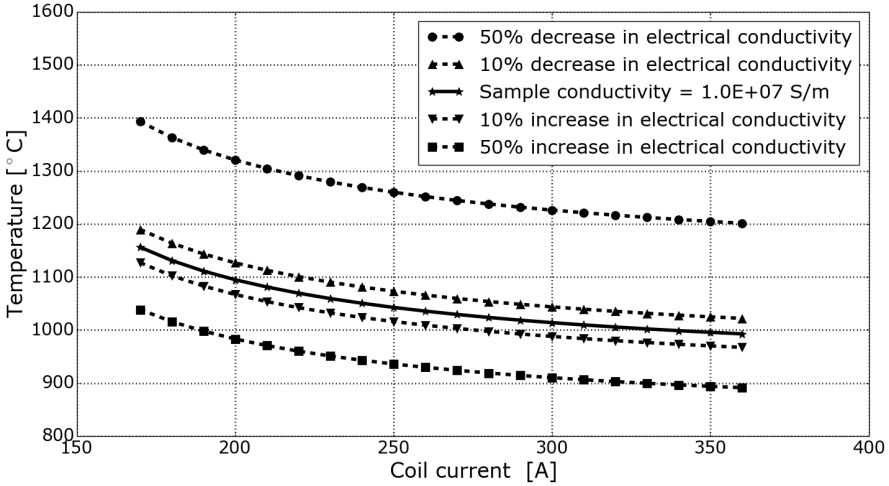

(e) Varying the electrical conductivity of the sample.

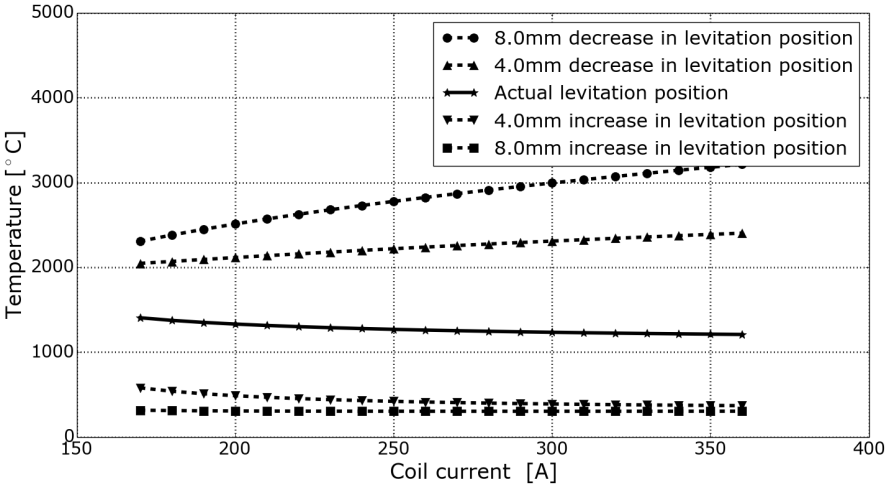

(f) Varying the stable levitation position of the sample.

Figure 4.12: Effect of changes in uncertain model parameters on the sample temperature as the coil current is increased.

increases with increasing coil current. To address the issue of the model predicting the sample to be too hot, the emissivity value used with the model is increased, resulting in increased heat loss from the modelled sample. As there is uncertainty about what the value of the sample emissivity should be, it should be reasonable to make adjustments to it. Figure 4.11b shows that the Royer et al. experimental results and current model prediction agree when an emissivity value of $\varepsilon = 0.21$ is used with the model. An emissivity value of $\varepsilon = 0.21$ is the expected emissivity value for heavily oxidized aluminium [3], and can realistically be the emissivity of a sample that is exposed to air before it is placed in the argon atmosphere of the levitation cell.

The model with the altered emissivity value successfully predicts the temperature values at low currents, where the measured sample temperature is decreasing with increasing coil current. However, it is clear that the model is unable to describe the increasing sample temperatures observed at higher current values. Royer et al. [14] report a similar limitation in their implementation of the simplified lumped parameter model of Fromm and Jehn [6]. Royer et al. [14] attributed this to the fact that the Fromm and Jehn [6] model does not take the spatial distribution of the absorbed power inside the sample into account. The current model implementation does however take this into account and it can therefore be ruled out as a possible cause for the difference between the model behaviour and experimental observations at large currents. We propose that the following possible reasons for this behaviour should be investigated further: the induced current in the sample might be saturating, it could be due to the fact that the temperature dependence of material properties are not taken into account by the model, or it is possible that the coil design has multiple stable levitation positions and the sample is levitated in a different position at higher coil currents.

4.2.4 Model validation conclusion

There are two parameters of interest in levitation cell modelling: the stable sample levitation position and the steady state sample temperature. In the modelling of both these parameters, the value of a number of properties required by the model are not known with certainty. Despite this, the model is still able to accurately predict the stable levitation zone inside a levitation cell. The levitation force along the central axis of the coil is also predicted successfully with calibration of the uncertain material properties. The sample temperature at low coil currents can be predicted with calibration of the uncertain properties in the heat transfer calculation, but the model is unable to predict the increasing sample temperatures at higher coil currents observed by Royer et al. [14]. Further investigation is necessary to determine the reason for this.

Chapter 5

Results & Levitation Cell Characterisation

5.1 Introduction

The purpose of the implemented levitation cell model is to make experimental work with the levitation cell more efficient through increasing our understanding of the levitation cell's operation. Changes in the coil geometry and electric current in the coil affect which sample sizes of which sample materials can be levitated and what the sample temperature will be. When it is calibrated, the levitation cell model could be used to determine if a specific coil design is suitable for a specific experiment and what operating parameters should be used for the experiment. Investigations with the model will contribute towards gaining better understanding of the behaviour of the levitation cell during operation.

5.2 Levitation cell case to be investigated

In order to illustrate the intended use of the levitation cell model, the levitation cell built at the University of Pretoria (shown in Figure 1.3) is modelled and its predicted behaviour during operation is investigated. There are two properties of this particular experimental setup that can easily be adjusted between experiments. The first adjustable property is the percentage power supplied to the coil which is directly proportional to the electric current in the coil. However, this experimental setup is not instrumented to measure the current in the coil which is currently a challenge for comparing model results to experimental results. The second adjustable property is the 'lid height' of the coil. The 'lid' of the coil refers to the top three coil loops of the levitation cell which are manufactured in such a way to allow for height adjustment as can be seen in Figure 1.3.

Since changes in the coil current and lid height are practically achievable in experiments, the model is used to investigate the effect of changes in these parameters on

the operation of the levitation cell. In each case two different sample sizes are investigated, with radii of 5 mm and 7 mm respectively, and also two different sample materials, namely aluminium and iron.

5.3 Input values

The input values used with the model for this investigation are:

- the geometry of the levitation cell available at the University of Pretoria as shown in Figure 1.3 and using the values in Table 5.1,
- the material properties of the aluminium and iron samples as given in Tables 4.3 and 4.1 respectively, and
- the material properties for an argon atmosphere around the sample as given in Table 4.1.

In all cases a $25 \times 25 \times 25$ mesh is used to discretise the spherical sample. The cell dimension in the radial direction decreases towards the outside of the sample to give a denser mesh close to the sample surface where field values with large gradients are expected due to the skin effect.

Table 5.1: Coil parameters used to model the levitation cell at the University of Pretoria.

Coil geometry

Loop nr	Radius r [m]	Height h [m]	Current direction, k
1	0.0081	0.0006	1.0
2	0.0083	0.0089	1.0
3	0.0085	0.0048	1.0
4	0.0088	0.0124	1.0
5	0.0091	0.0163	1.0
6	0.0109	0.0202	1.0
7	0.0141	0.0243	1.0
8	0.0164	0.0289	1.0
9	0.0172	0.0334	1.0
10	0.0134	0.0398	0.0
11	0.0135	0.0492	0.0
12	0.0135	0.0443	0.0

Coil properties

Property	Value
Coil current	100 A
Frequency	179 kHz
Tube radius	0.003 m

Since experimental work is excluded from the scope of the current project, experiments were not done to calibrate the model. In this investigation conclusions can therefore only be made about the trends resulting from changes in coil current and lid height, and not about the specific values predicted by the model.

5.4 Increasing the coil current

5.4.1 Aluminium sample

Figure 5.1 shows the variation of the levitation force acting on an aluminium sample along the central axis of the coil given in Figure 1.3. Comparing the plot for a sample with a radius of 5 mm in Figure 5.1a to that of sample with a radius of 7 mm in Figure 5.1b, it is seen that a larger sample size results not only in a larger sample weight, but also in a larger levitation force at a specified coil current. A coil current of 100 A would not be enough to levitate either of the 5 mm or 7 mm radius samples, but in both cases increasing the current to 150 A would allow for levitation. Therefore, it seems that the coil current required to levitate a sample does not depend on sample size. It can further be seen that the stable levitation position moves higher up in the coil as the coil current is increased. The stable levitation position is the position inside the coil where the levitation force is equal to the sample weight, and the gradient of the levitation force is negative.

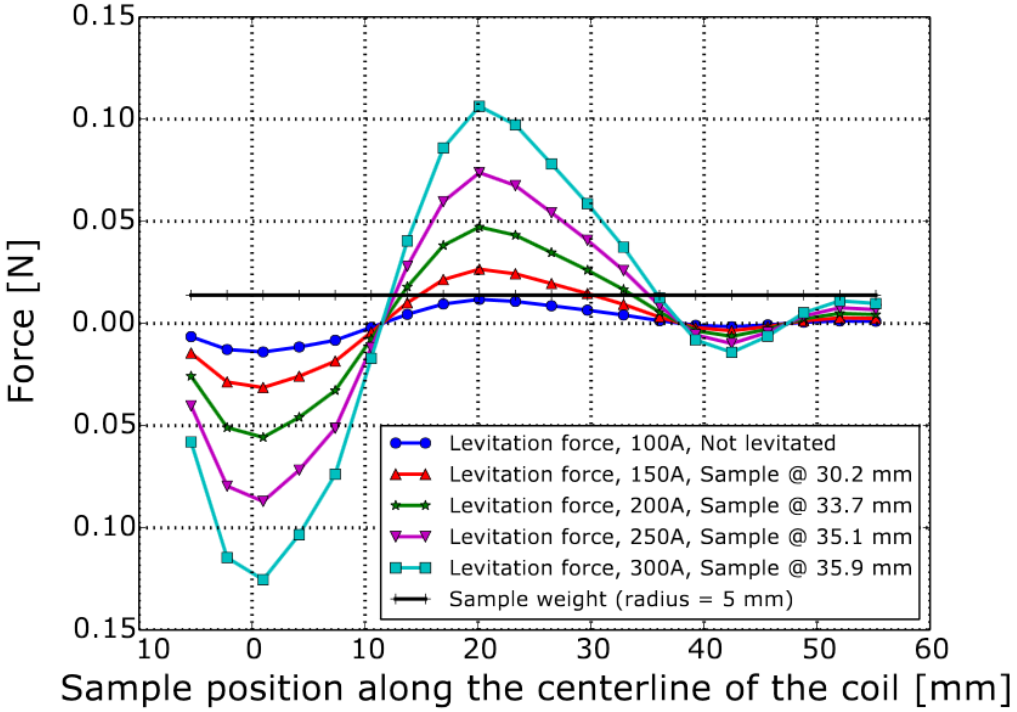

(a) Sample radius = 5 mm.

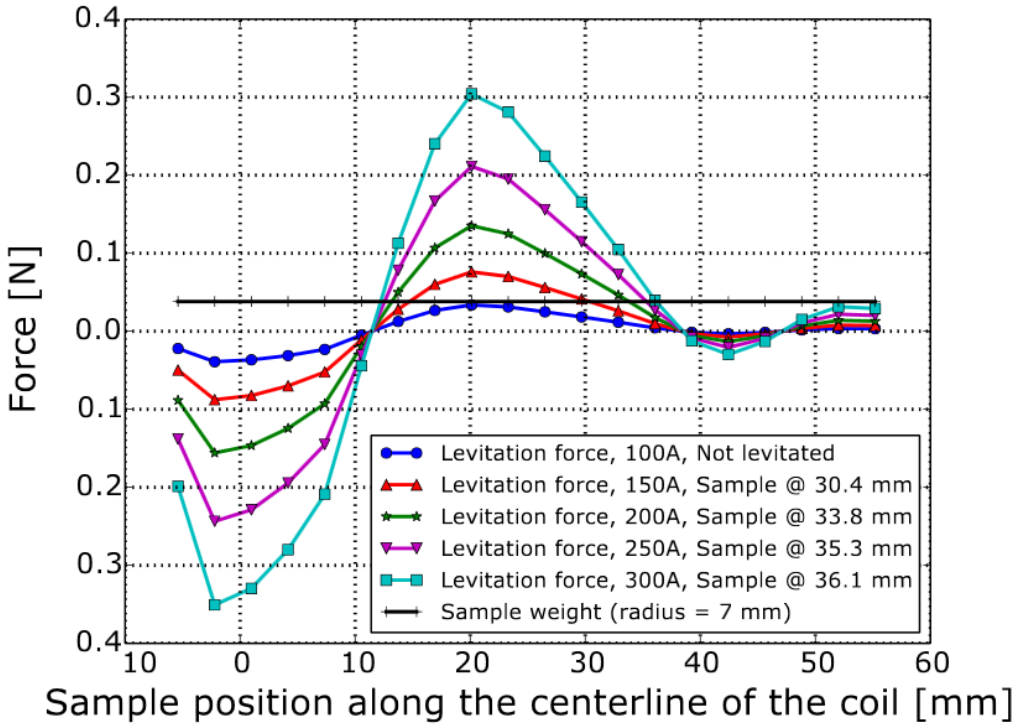

(b) Sample radius = 7 mm.

Figure 5.1: Levitation force with increasing coil current for aluminium samples.

Figure 5.2 show the effect of an increase in coil current on the sample temperature, only for the cases where the coil current is large enough to levitate the sample. The

sample temperature decreases to a minimum at 200 A and from there on increases with increasing coil current for both sample sizes. The larger sample is heated to a higher temperature than the smaller sample.

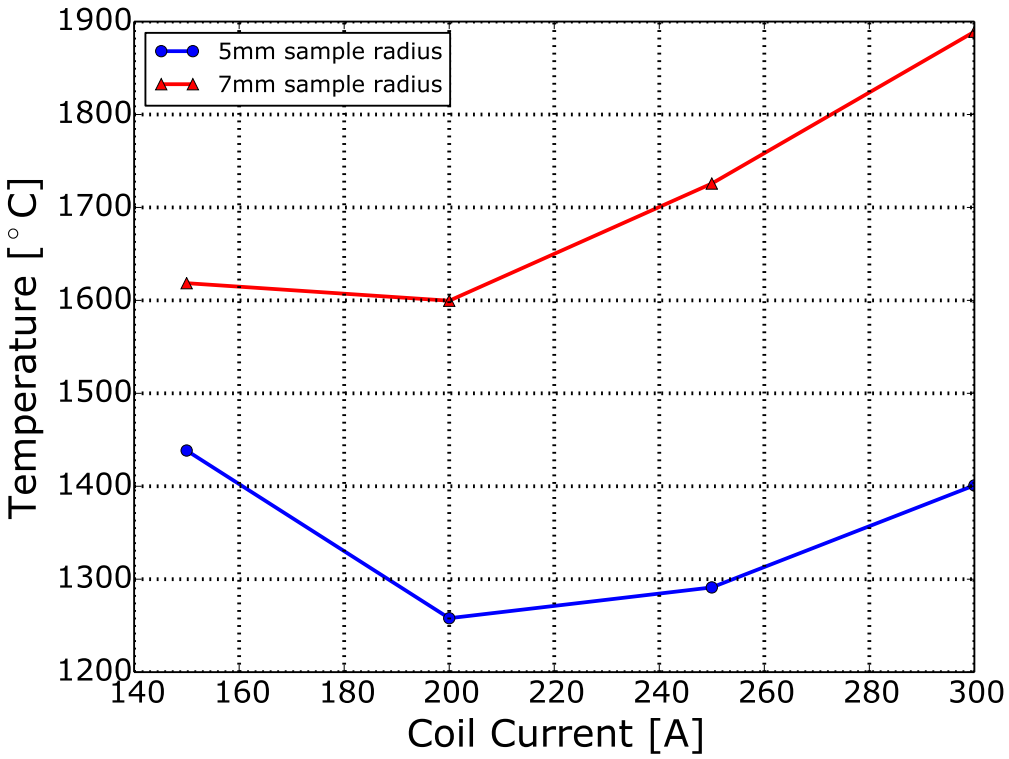

Figure 5.2: Temperature of levitated aluminium samples with increasing coil current.

5.4.2 Iron sample

Figure 5.3 shows the predicted levitation force and sample weight for an iron samples with radii of 5 mm and 7 mm. The levitation force is larger for the larger sample size, as was the case with aluminium sample in Figure 5.1. Again, the stable levitation position is also higher up inside the coil for increased coil currents. Since iron has a larger density than aluminium, a larger coil current is required to levitate an iron sample than an aluminium sample of the same size. The coil current required to levitate a specific sample is therefore determined by the sample material, but not by the sample size.

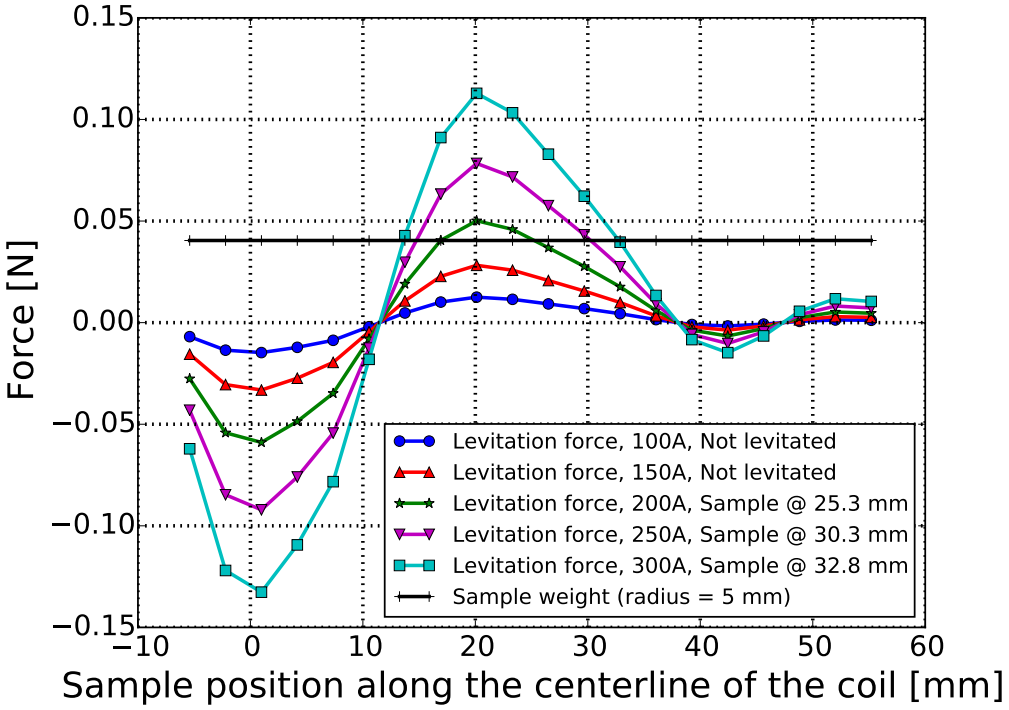

(a) Sample radius = 5 mm.

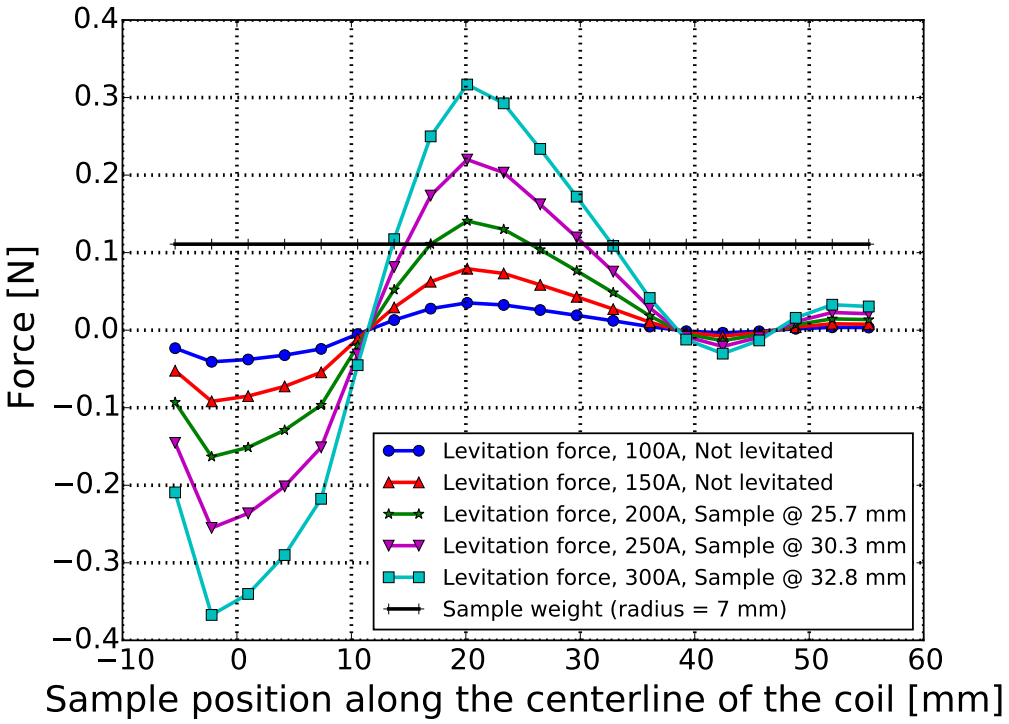

(b) Sample radius = 7 mm.

Figure 5.3: Levitation force with increasing coil current for iron samples.

Figure 5.4 shows that the temperature of the levitated iron samples decreases with increasing coil current. The larger sample again has a larger temperature.

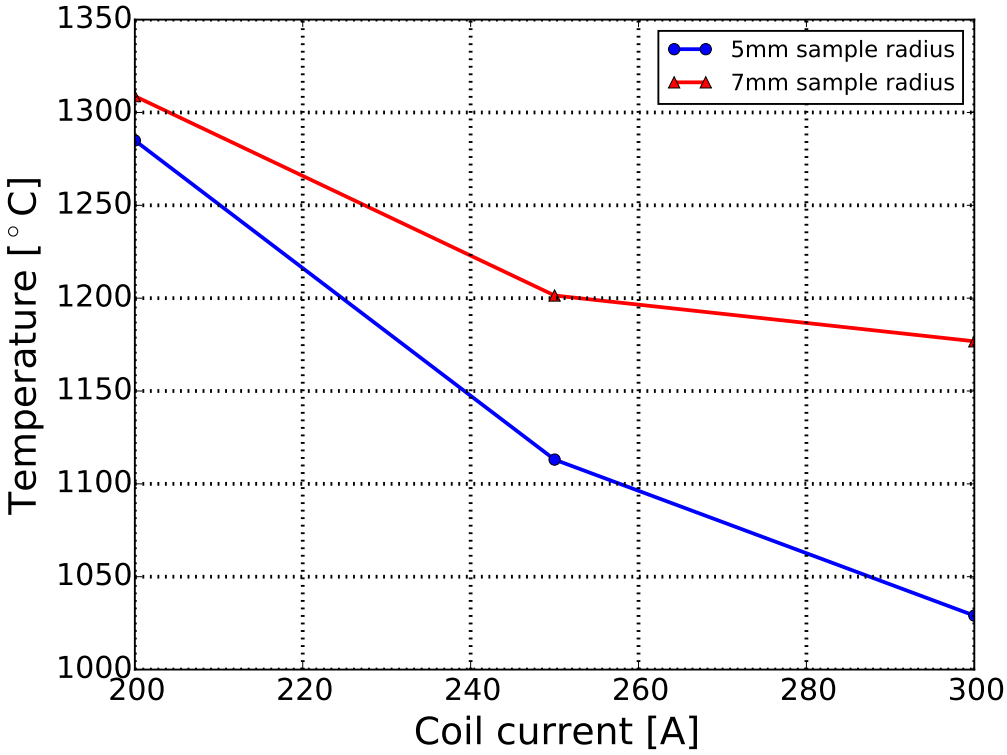

Figure 5.4: Temperature of levitated iron samples with increasing coil current.

5.4.3 Fields inside the sample at different coil currents

Since the electromagnetic part of the implemented model is a distributed parameter model, the model can visualise the predicted current-, power-, magnetic-, and levitation force inside the sample. Figure 5.5 shows these predicted fields inside aluminium samples with a radius of 5 mm. The figures on the left are for a coil current of 150 A, and the figures on the right are for a coil current of 300 A. Due to the axisymmetric assumption in the model, only one symmetric half of a cross-section through the sample is shown.

It is clear from the field plots in Figure 5.5 that most of the effects occur close to the surface of the sample. This is due to the skin effect that is described in Section 3.3.1. The gradient across the levitation force field is significantly larger for the 300 A case than for the 150 A case. In the 150 A case there is a variation in force values of 0.00175 N/mm^3, while the levitation force across the sample varies with 0.0032 N/mm^3 for a coil current of 300 A. This means that the molten droplet will be more deformed from its original spherical shape, and more stirring will occur with a larger coil current. If less stirring is required, it is recommended to levitate the sample using a coil current just large enough to allow for levitation, while a large coil current should be used is more stirring if required.

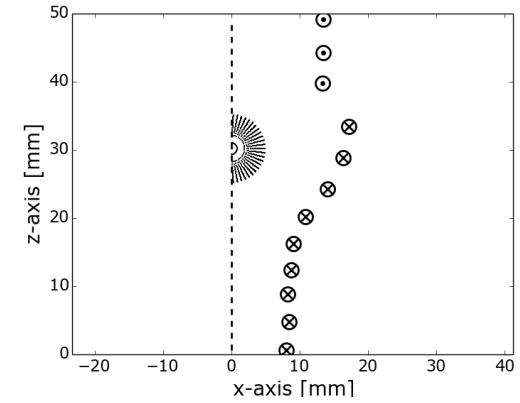

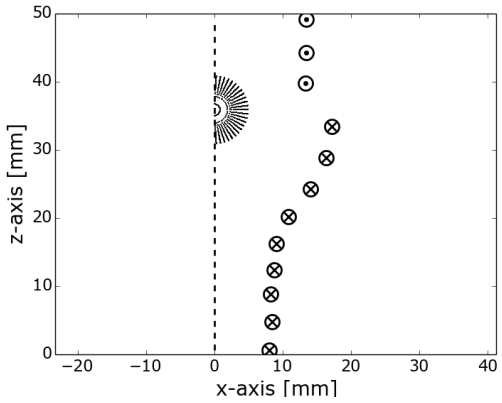

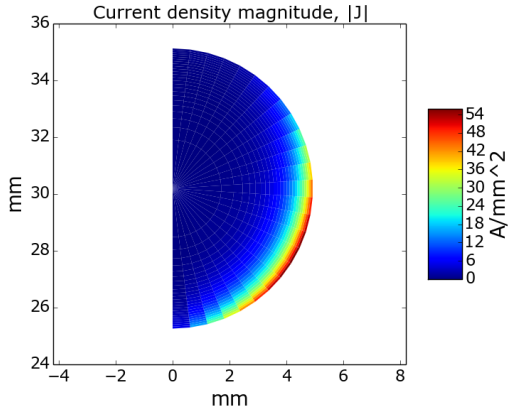

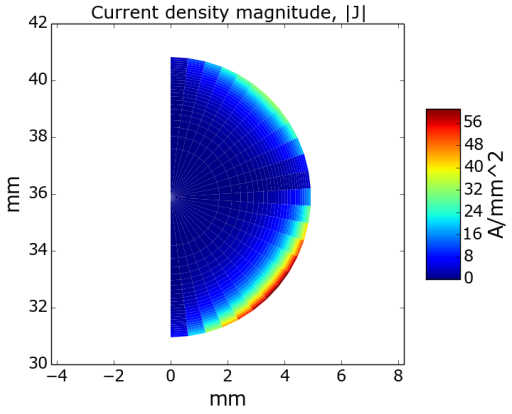

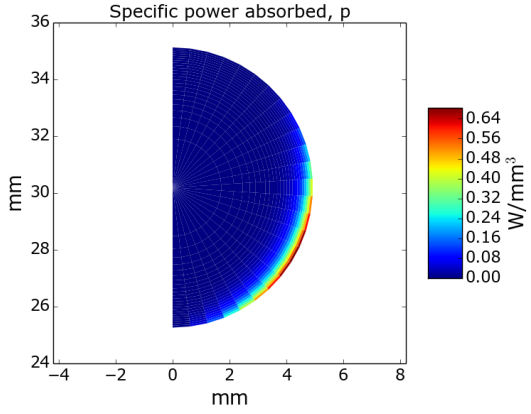

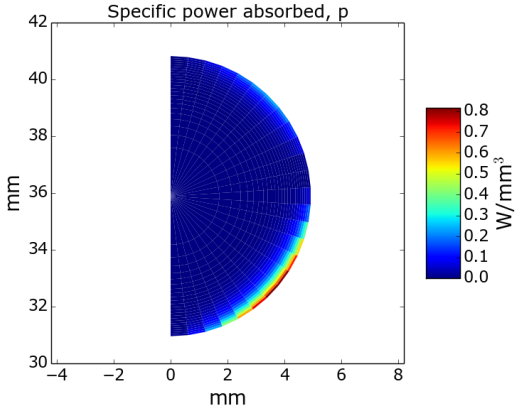

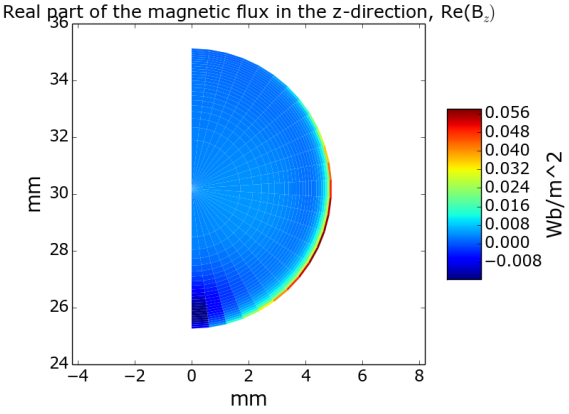

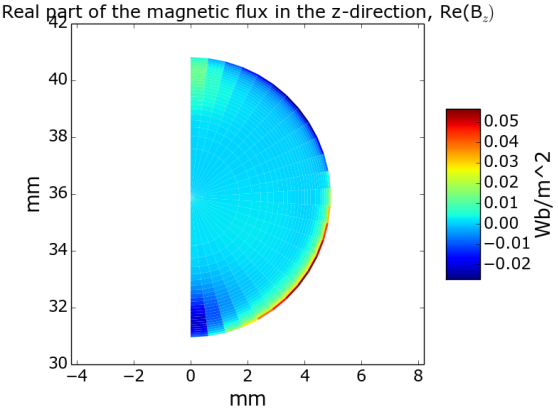

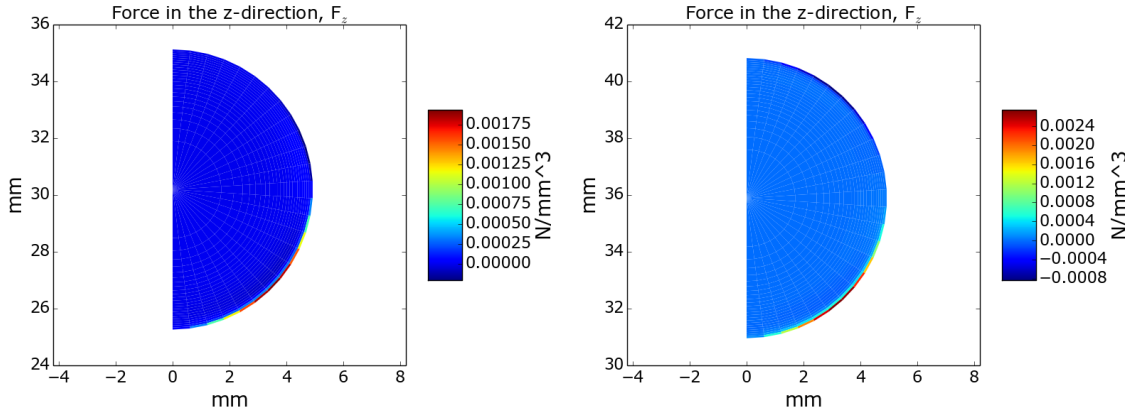

Figure 5.5: Fields inside the levitated sample. Figures on the left are for a coil current of 100 A and figures on the right for a coil current of 300 A.

5.5 Moving the lid

5.5.1 Aluminium sample

Figure 5.6 shows the levitation force along the center of the coil for a aluminium sample when the coil lid is positioned at different increased heights from its initial position given in Table 5.1. It can be seen that the levitation force is only affected slightly in the region of the lid when it is moved upwards. This effect is more significant for the larger sample size that generally has a larger levitation force associated with it. As the lid is moved higher up, the stable levitation position also moves slightly higher. This is because moving the lid upwards, decreases the influence of the lid's magnetic field on the magnetic field of the bottom coil and consequently decreases the gradient of the levitation force in the region between the bottom coil and the lid. As a result the axial position where the levitation force is equal to the weight of the sample is now in a higher location. Another consequence of the decreased force gradient when the coil lid is in a higher position, is that levitation force is now less self-correcting for deviations in sample position, resulting in a levitation position that is less stable.

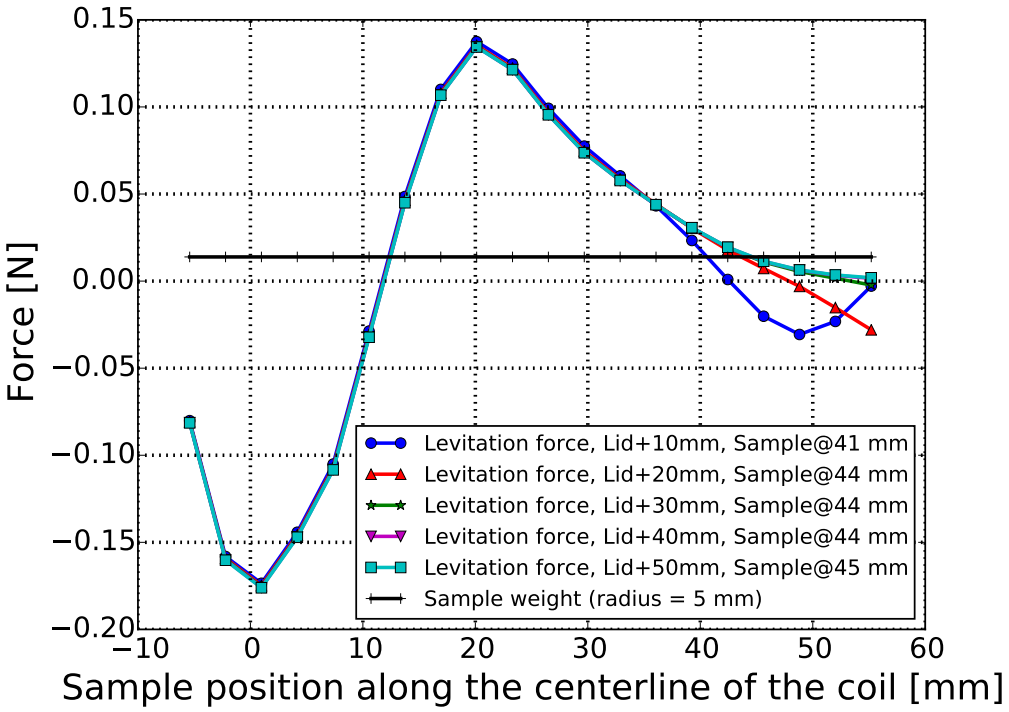

(a) Sample radius = 5 mm.

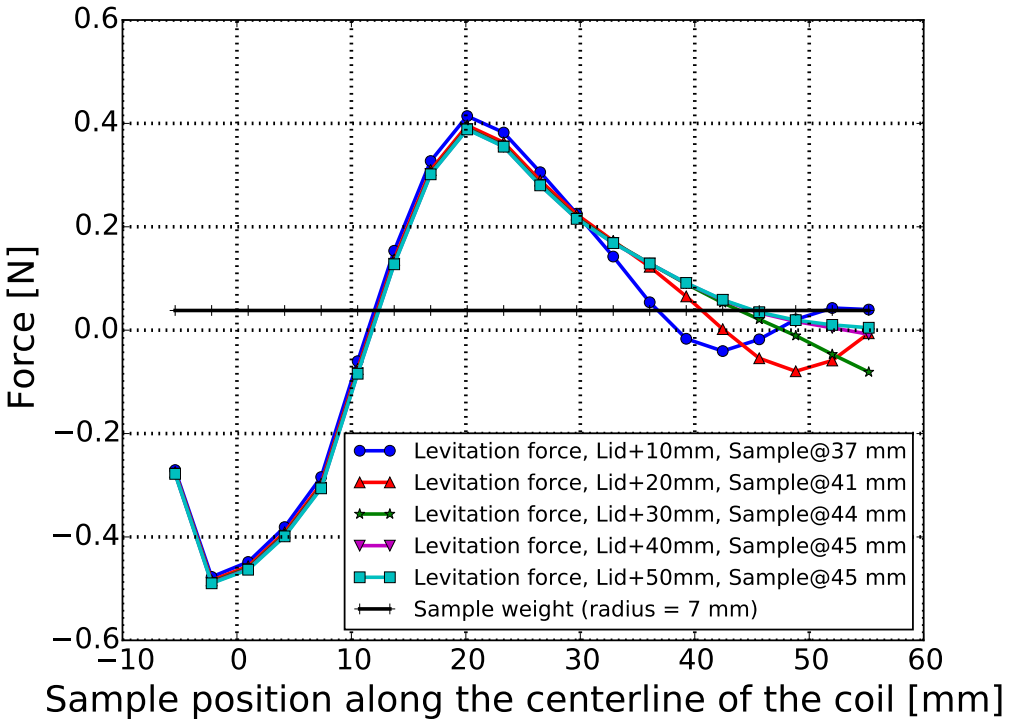

(b) Sample radius = 7 mm.

Figure 5.6: Levitation force with increasing lid height for aluminium samples.

Figure 5.7 shows the the predicted variation in sample temperature as the coil lid is moved upwards. The temperature is very nonlinear and if the lid is moved far

away from the sample it has a smaller effect on the sample temperature. However, the graph suggests that a movable coil lid allows for access to a significant range of sample temperatures.

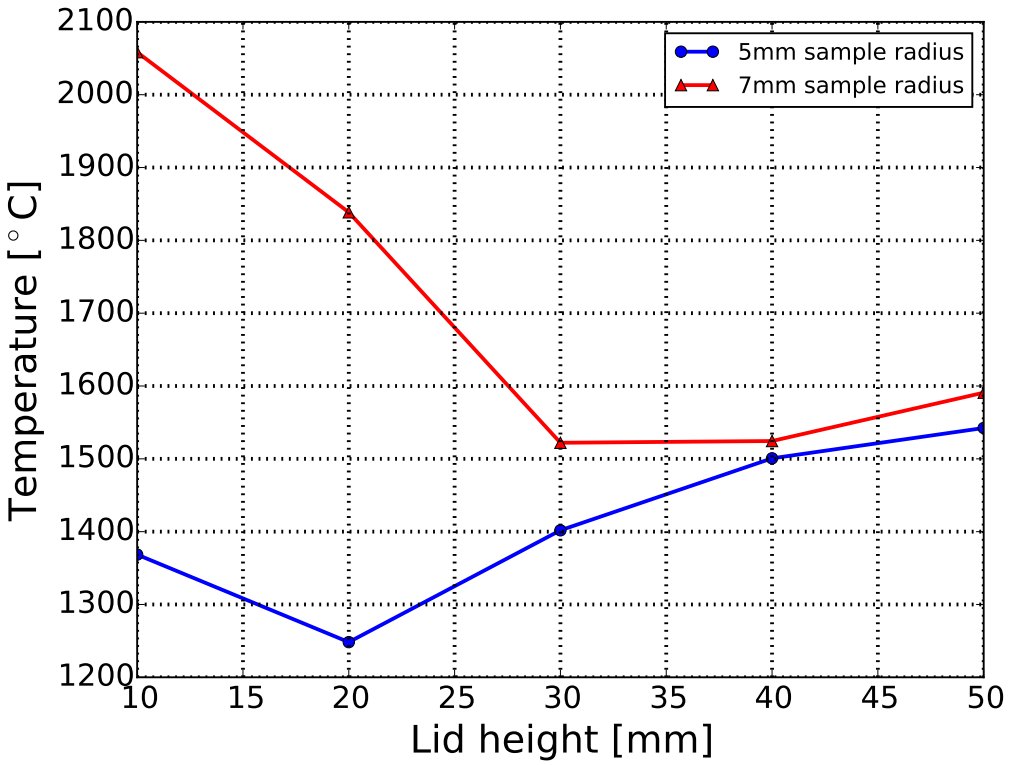

Figure 5.7: Temperature of levitated aluminium samples with increasing lid height.

5.5.2 Iron sample

Moving the lid with an iron sample shows similar behaviour as with an aluminium sample as can be seen in Figure 5.8.

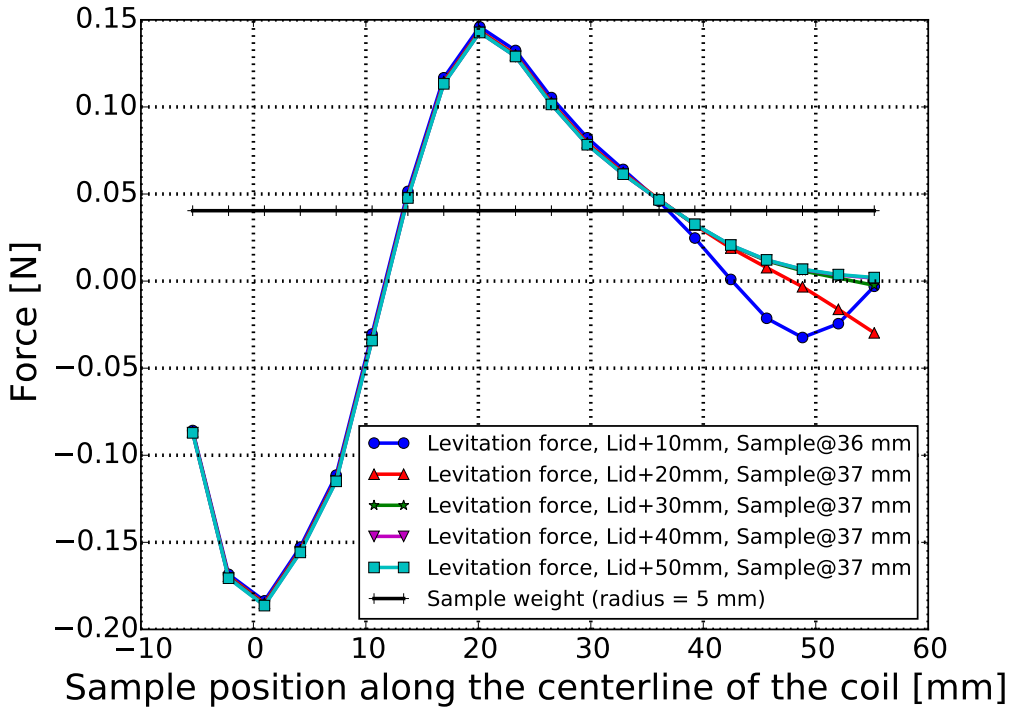

(a) Sample radius = 5 mm.

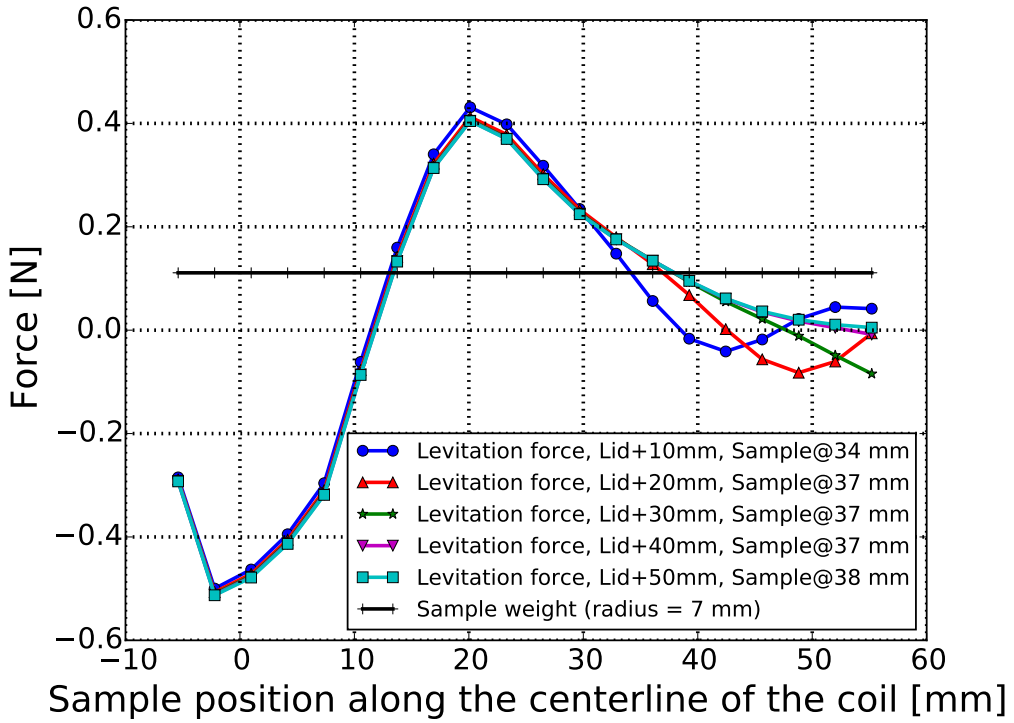

(b) Sample radius = 7 mm.

Figure 5.8: Levitation force with increasing lid height for iron samples.

The effect on the temperature of an iron sample while moving the coil lid is given in Figure 5.9. Moving the coil lid also allows for variation in temperature with an iron

sample, but less so than for an aluminium sample. In the case of the iron sample, sample size does not have a large effect on the sample temperature.

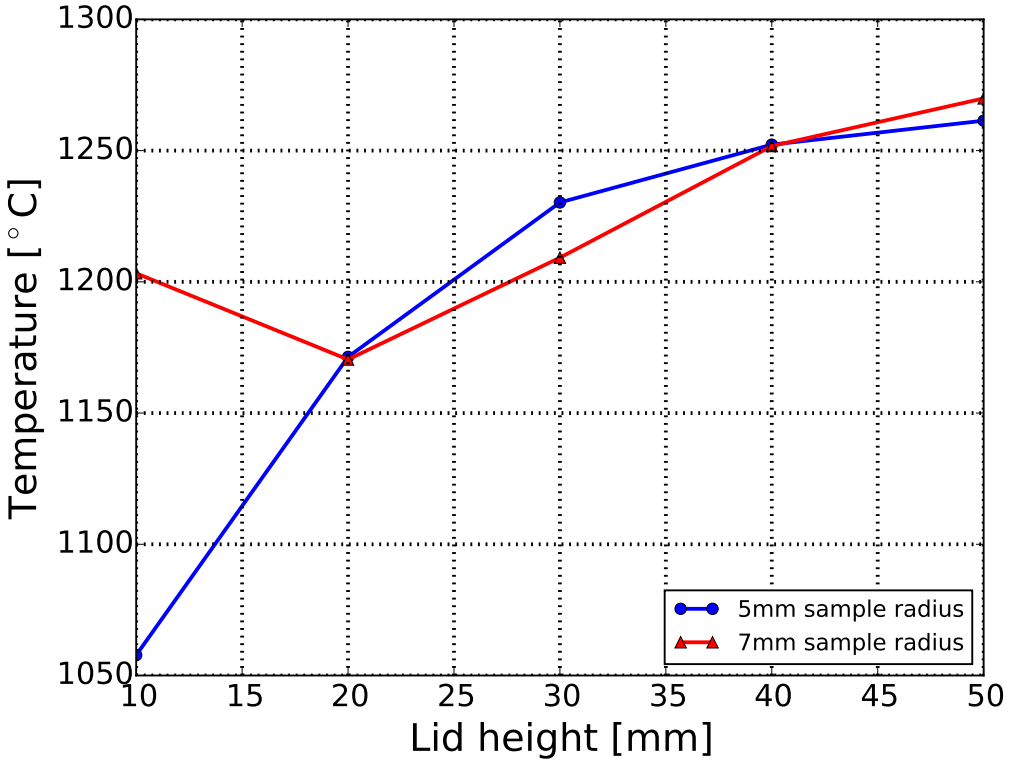

Figure 5.9: Temperature of levitated iron samples with increasing lid height.

5.5.3 Fields inside the sample at different lid heights

The fields inside an 5 mm radius, aluminium sample levitated at different lid heights are given in Figure 5.10. The fields look very similar at the two lid heights except that the influence of the lid in its configuration closer to the sample can be seen in the induced current field, and the absorbed power values are higher when the lid is closer to the sample, which is also the cause of the higher sample temperature.

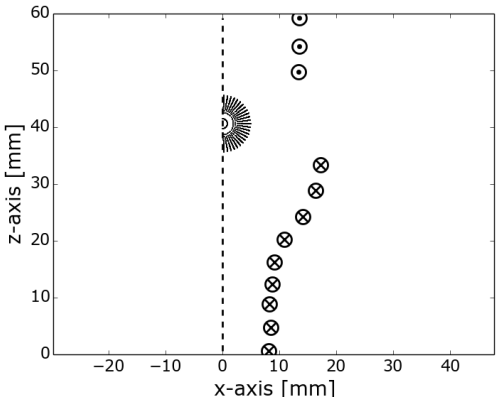

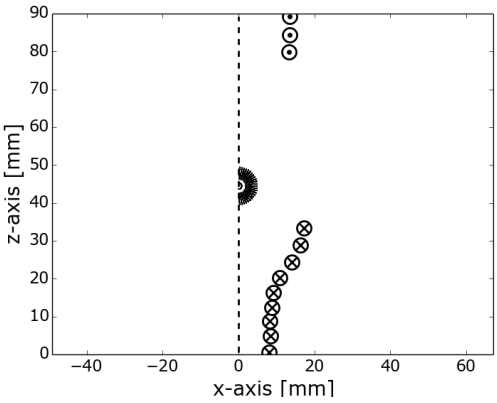

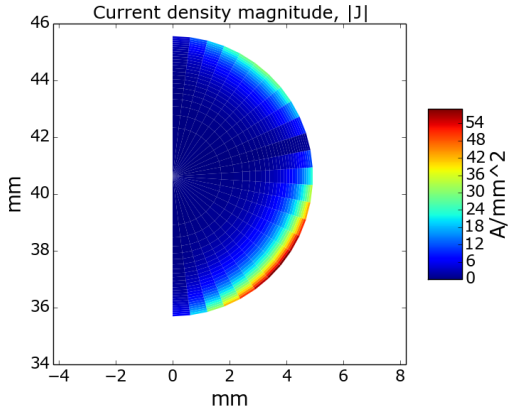

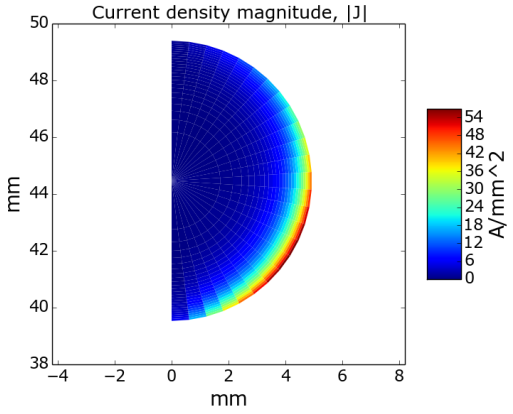

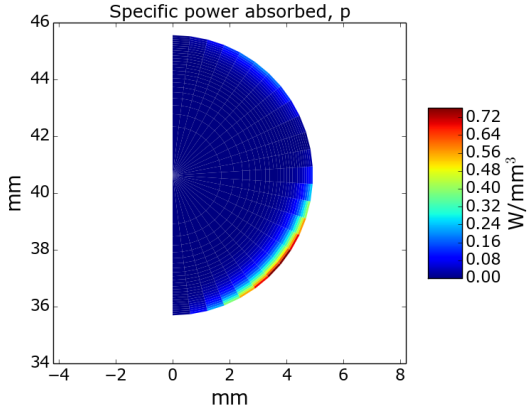

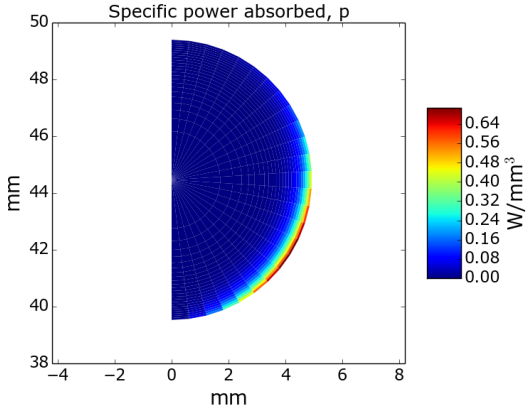

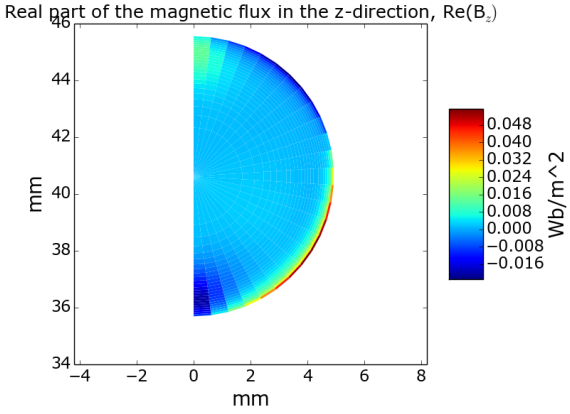

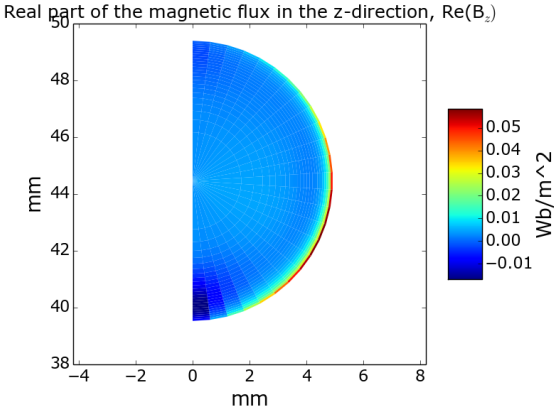

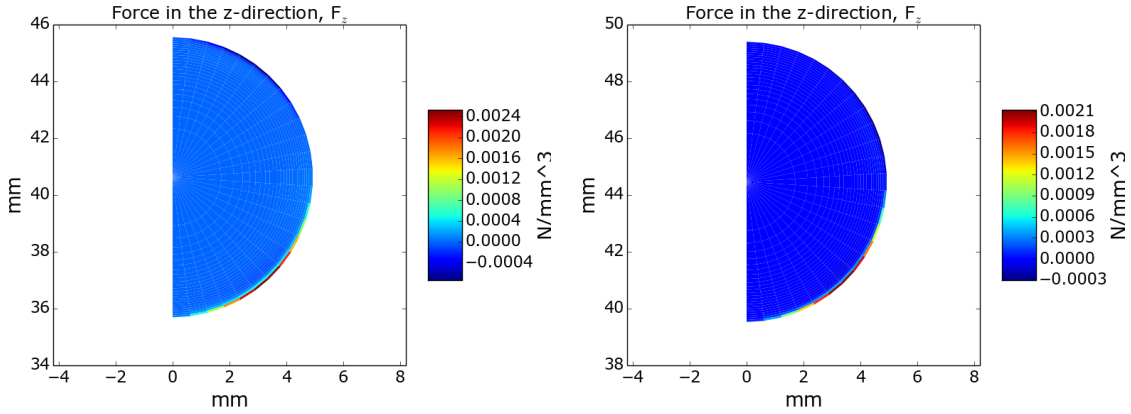

Figure 5.10: Fields inside a 5 mm radius, aluminium levitated sample. Figures on the left are for a lid height of 10 mm and figures on the right for a lid height of 50 mm.

5.6 Levitation cell operation recommendations

The model is used to determine the effect that changes in the coil current and lid height would have on a levitated sample and how this can possibly used to control experiments. The available experimental setup has the limitation that it is not instrumented to measure coil current, but although the specific current value is not known during an experiment, it is still possible to increase or decrease the coil current by increasing or decreasing the percentage power provided to the coil from the power supply. From the levitation force plots presented in this chapter (Figures 5.1 and 5.3) it is clear that a there is a minimum coil current magnitude required to levitate a specific sample material. A larger coil current is required to levitate materials with larger densities. To determine the percentage power that would be required to levitate a specific sample material, it is recommended to start by attempting to levitate a sample at a low percentage power. The power supplied to the coil can then gradually be increased until the current is sufficient to successfully levitate the sample. Once the required power setting for a material is found, the results in this chapter shows that is should be possible to levitated spherical sample of any size at the power setting, as long as they are all of the same material.

Changes in the coil current, lid height as well as sample size all result in changes in sample temperature. However, larger coil currents result in larger force gradients across the sample and increased sample deformation and stirring inside the molten droplet. Moving the lid does not have a significant effect on the forces acting on the sample, but it does affect the sample temperature.

Chapter 6

Conclusion and Recommendations

6.1 Conclusion

This dissertation describes the implementation of a numerical model of an electromagnetic levitation cell, and its use in characterising the behaviour of the levitation cell in order to increase understanding of the levitation cell operation and provide support for experimental studies that make use of the levitation cell. The behaviour of the levitation cell is modelled with a distributed parameter electromagnetic model combined with a lumped parameter heat transfer model. The electromagnetic model is based on the model described by El-Kaddah & Szekely [4], but some modifications are made to the model. The heat transfer model is limited to a lumped parameter model because it is found that heat conduction inside the sample occurs at a much faster rate relative to the convection and radiation heat loss from the sample as described by the Biot number. This results in a negligible temperature gradient inside the sample, and therefore a lumped parameter model suffices.

As the intended use for the model is to support electromagnetic levitation experiments, care is taken to verify and validate the model implementation. A simple levitation cell case for which there exists a similar case with an analytical solution is described and used to verify the electromagnetic model implementation. The electromagnetic model is validated by comparing levitation force predictions for a single loop coil to experimental force measurements published by Fromm & Jehn [6]. It is found that force predictions from the model agree with experimental results once the model is calibrated. Proposed experimental investigations using the levitation cell include using it to obtain high temperature material properties, as these properties are seldom available in literature and difficult to obtain experimentally due sample contamination by the container. As a result uncertainty exists around the high temperature values of the material properties used in the levitation cell model. It is therefore suggested that these material properties are adjusted in order to calibrate the model. The heat transfer part of the model is validated by comparing predicted sample temperatures at different coil currents to the experimentally measured tem-

peratures of Royer et al. [14]. The model is found to accurately predict sample temperatures at low coil currents but not at higher currents. Further investigation is required to determine why this is the case.

The implemented model is used in sensitivity studies to investigate the effect of changes in the uncertain high temperature material property values. The location of the stable levitation region is found to be independent of the material property values. It is therefore possible to use the model to design levitation cells for stable levitation without knowledge of the exact values of the high temperature material properties that should be used in the model. The designed levitation cell could then be used in experiments to determine high temperature material property values, which would in turn improve the model. The improved model can then potentially be used to design levitation cells for more properties than just stability.

The levitation cell model is used to investigate the effect of changes in the coil current and the position of the coil lid. It is found that larger coil currents are required to levitate sample materials of higher densities. Coil current does not influence the size of the spherical samples that can be levitated. Since there is a minimum coil current required to levitate a sample of a specific material it is recommended that experiments with levitation cells that are not instrumented to measure coil current are started at the lowest power setting and power is increased until the sample is successfully levitated. This power setting can then be used to levitate samples of any size as long as they are of the same material. Model results show that an increase in coil current results in a larger force gradient across the sample. A larger force gradient would increase stirring inside the molten droplet and cause it to deform more from its original spherical shape than when a smaller coil current is used. Changes in the coil lid height do not have a significant influence on the levitation force, but do affect the sample temperature. Apart from changing the lid height, the model predicts that coil current and sample size can also be used to control the sample temperature during experiments.

This work therefore makes the following contributions towards the modelling of electromagnetic levitation cells:

- a more computationally efficient implementation of the electromagnetic part of the levitation cell model described by El-Kaddah & Szekely is described and implemented,
- the parallel ring test is described as a verification test for the levitation force predicted by a levitation cell model,
- the levitation force predicted by the model of El-Kaddah & Szekely is shown to agree with experimental results once it is model is calibrated,
- it is shown that it is possible to design levitation cells for stable levitation without precise knowledge of the high temperature material property values used in the model or the magnitude of the electrical current in the coil,
- an investigation using the model shows that increasing the coil current will increase the deformation of, and stirring inside a levitated, molten droplet,

and

- the temperature of the levitated sample can be adjusted by changing the height of the coil lid, increasing the coil current of varying the sample size.

6.2 Recommendations for future work

The scope of the current work does not include experimental work, but it is recommended that levitation cell experiments with increasing coil current and different lid positions is done. A comparison can then be done between the experimental findings and the model findings presented here. Specifically, this work makes the following two testable predictions that should be investigated experimentally:

1. numerical investigations using the model predicts that spherical samples of the same material but different sizes should levitate at the same power setting, and
2. model investigations predicts that moving the coil lid only has a small effect on the levitation force and levitation position of the sample, but does significantly affect the sample temperature.

Future work should also include an investigation to determine why the model temperature predictions differ from experimental measurements published by Royer et al. [14] at high temperatures.

The model can further be used with an optimization algorithm to develop a levitation cell design tool. The design tool will determine the coil geometry and current required to levitate a sample of a specified material and size to a specified temperature. Royer et al. [14] used the model described by Fromm & Jehn [6] with a genetic-like optimization algorithm to design levitation cells to minimize the sample temperature. However, the current model is more accurate than that of Fromm & Jehn [6] for describing multi-loop coils and it is therefore proposed it would be better suited for use in an levitation cell design tool.

Bibliography

[1] Piero Bassanini and Alan Elcrat. Mathematical theory of electromagnetism. SIMAI e-Lecture Notes, 2009.

[2] Richard L. Burden and J. Douglas Faires. *Numerical Analysis*. Richard Stratton, 9th edition, 2011.

[3] Yunus A. Çengel. *Heat and Mass Transfer - A Practical Approach*. McGraw-Hill, 2006.

[4] N El-Kaddah and J Szekely. The electromagnetic force field, fluid flow field, and temperature profiles in levitated metal droplets. *Metallurgical Transactions B*, 14(3):401–410, 1983.

[5] Lin Feng and Wan-Yuan Shi. The influence of coil angle arrangement on dynamic deformation and stability of molten droplet in electromagnetic levitation system. *ISIJ International*, 56(1):50–56, 2016.

[6] E. Fromm and H. Jehn. Electromagnetic forces and power absorption in levitation melting. *British Journal of Applied Physics*, 16:653 – 659, 1965.

[7] David J. Griffiths. *Introduction to Electrodynamics*. Prentice Hall, 1999.

[8] A. Kermanpur, M. Jafari, and M. Vaghayenegar. Electromagnetic-thermal coupled simulation of levitation melting of metals. *Journal of Materials Processing Technology*, 211:222–229, 2011.

[9] G. Lohöfer. Theory of an electromagnetically levitated metal sphere i: Absorbed power. *SIAM Journal on Applied Mathematics*, 49(2):567–581, April 1989.

[10] ZA Moghimi, M Halali, and M Nusheh. An investigation on the temperature and stability behavior in the levitation melting of nickel. *Metallurgical and Materials Transactions B*, 37(6):997–1005, 2006.

[11] Otto Muck. Verfahren und vorrichtung zum schmelzen, insbesondere von leitern u. dgl. durch elektrische induktionsstroeme, November 23 1925. DE Patent 422,004.

[12] E.C. Okress, D.M. Wroughton, G. Comenetz, P.H. Brace, and J.C.R. Kelly. Electromagnetic levitation of solid and molten metals. *Journal of Applied Physics*, 23(545), 1952.

[13] Simon Ramo, John R. Whinnery, and Theodore Van Duzer. *Fields and Waves in Communication Electronics*. John Wiley & Sons, Inc., 1994.

[14] Z. L. Royer, C. Tackes, R. LeSar, and R. E. Napolitano. Coil optimization for electromagnetic levitation using a genetic like algorithm. *Journal of Applied Physics*, 113:214901–1 – 214901–9, 2013.

[15] William R. Smythe. *Static and Dynamic Electricity*. McGraw-Hill, 1950.

[16] Julian Szekely. *Fluid Flow Phenomena in Metals Processing*. Academic Press, Inc., 1979.

[17] Erach D. Tarapore and James W. Evans. Fluid velocities in induction melting furnaces: Part 1. theory and laboratory experiments. *Metallurgical Transactions B*, 78:343–351, 1976.

[18] B.L. Zink, A.D. Avery, R. Sultan, D. Bassett, and M.R. Pufall. Exploring thermoelectric effects and wiedemann-franz violation in magnetic nanostructures via micromachined thermal platforms. *Solid State Communications*, 150:514–518, 2010.

[19] Jin-Ho Zong, Julian Szekely, and Elliot Schwartz. An improved computational technique for calculating electromagnetic forces and power absorptions generated in spherical and deformed body in levitation melting devices. *Transactions on Magnetics*, 28(3):1833 – 1842, May 1992.